SCALABLE TACTILE SENSING E-SKINS THROUGH SPATIAL FREQUENCY ENCODING

by
Ariel Slepyan

A thesis submitted to Johns Hopkins University in conformity with the requirements for

the degree of Master of Science and Engineering

Baltimore, Maryland

August 2021

Abstract

Most state-of-the-art tactile sensing arrays are not scalable to large numbers of sensing units due to their raster-scanned readout. This readout scheme results in a high degree of wiring complexity and a tradeoff between spatial and temporal resolution. In this thesis I present the use of spatial frequency encoding to develop asynchronous tactile sensor arrays with single-wire sensor transduction, no per-taxel electronics, and no scanning latency. I demonstrate this through two prototype devices, Neuroskin 1, which is developed using fabric-based e-textile materials, and Neuroskin 2, which is developed using fPCB. Like human skin, Neuroskin has a temporal resolution of 1 kHz and innate data compression where tactile data from an MxN Neuroskin is compressed into M+N values. Neuroskin 2 requires only four interface wires (regardless of its number of sensors) and can be easily scaled up through its development as an fPCB. To demonstrate the utility of the prototypes, Neuroskin was mounted onto a biomimetic robotic finger to palpate different textures and perform a texture discrimination task. Neuroskin 1 and 2 achieved 87% and 76% classification accuracy respectively in the texture discrimination task. Overall, the method of spatial-frequency encoding is theoretically scalable to support sensor arrays with thousands of sensing elements without latency, and the

resolution of a Neuroskin array is only limited by the ADC sampling rate. Future tactile sensing systems can utilize the spatial frequency encoding architecture presented here to be dense, numerous, and flexible while retaining excellent temporal resolution.

Primary Reader and Advisor: Nitish V. Thakor, PhD

Secondary Reader: James E. West, PhD

Secondary Reader: Jeremy D. Brown, PhD

Dedication

I am dedicating this thesis to my mom, sister, and dad.

Contents

List of Tables

List of Figures

Motivation

Research in tactile sensing has enabled many advances in robotics and prosthetics. This is largely because tactile sensors have granted a 'sense of touch' to robotic devices. For upper limb prosthetics, tactile sensors have been developed to cover the fingertips, palm, or other parts of the prosthetic limb to measure pressure and force for sensory feedback. For lower limb prosthetics, they have been used to cover foot soles to help with sensory feedback for gate improvement. Overall, the incorporation of tactile sensors into prosthetic limbs has been shown to greatly help prosthesis users handle everyday objects and navigate their environments.

In addition to prosthetic devices, tactile sensors have had a significant impact on other fields of robotics, such as in manufacturing/assembly, autonomous navigation, humanoid robotics, and bio-inspired robots. For example, the first artificial tactile sensing array was developed for industrial parts handling equipment. Since then, tactile sensors have been used for robotic systems involved in grasping and manipulation to provide force feedback. This is particularly useful for applications where delicate grasping is desired. These sensors 'close the loop' for grasping robots and enable the development of precise control systems.

Despite these great applications, current tactile sensing systems are not scalable to support a large number of sensing elements. This is a major limitation for developing

full-body tactile sensing 'skins', or for the development of very high-density tactile sensing arrays.

The goal of this work is to overcome this limitation by developing a new, scalable tactile sensing system that can support the next generation of smart robotic devices.

Foreword on touch

The sense of touch is ubiquitous throughout biology [1]. All organisms use a form of touch to sense their environment, and to help inform them on how to best interact with the world [1]. Humans and other mammals have especially sophisticated touch, with many distributed mechanoreceptors and various adaptation mechanisms [2]; but even unicellular organisms such as the *Paramecium* will respond to mechanical perturbations of its outer membrane [3].

For single cell organisms such as this *Paramecium,* touch is sensed through microscopic hairs called cilia [3]. These cilia cover the entire body of the *Paramecium* and beat in a periodic way to induce thrust and motion through the organism's environment (Figure 0.1). When pressure is applied to the cilia, ion currents are induced in the cell, triggering the beating of the cilia, and directing the *Paramecium* away from the stimulus [3].

Figure 0.1: Phase contrast photomicrographs of a Paramecium caudatum. (Main) Anterior tip of the organism, showing hundreds of cilia (hair-like appendages) sprouting from its surface. Scale bar: 10μm. (Inset) Lower magnification view showing the whole organism. Scale bar: 25μm. Reprinted from [4].

These cilia are the most primitive, and most general, structures used to sense mechanical stimuli throughout biology. Multicellular organisms, such as sponges, are one of the earliest evolving phyla after the unicellular organisms and have an array of cilia [5]. When arrays of cilia are formed, they enable organisms to obtain spatiotemporal information about mechanical stimuli. For example, these cilia arrays give sponges a sense of flow direction [5].

As life evolved and became more sophisticated, and multicellular, these sensing arrays evolved as well. Plant life evolved after multicellular organisms, and although we may not think of plants as sensitive to touch, plants use mechanosensation to guide how they mature, grow, and change with time [6]. In modern plants, there are two classes of mechanical responses which can be described as rapidly moving and slowly moving [6]. The slowly moving class is responsible for life-long, developmental shaping and structuring of the plant. This class enables vines to grow around poles and branches, and complex root systems to grow through cracks in the sidewalk or asphalt. Humans often exploit this adaptation when designing bonsai trees or landscaping. The rapidly moving class is responsible for extremely rapid movements in response to touch – this is observed in the snapping trap of the Venus flytrap (*Dionaea muscipula)* or the rapid folding of fern *Mimosa pudica* [6]. In the case of the venus fly trap, when insects bump into the 'trigger' hairs on the ventral leaf surface, intercellular electrical signals are generated (ion currents), triggering differential enlargement of lobe cells and closing of the trap [6]. As different receptors are triggered in the trap, dynamic changes in cell expansion are triggered evoking the different stages of the trap [6]. This adaptation allows small insects

to escape before the trap is fully closed (not worth the plant's energy), but signals for full trap closure when the insects are large (Figure 0.2).

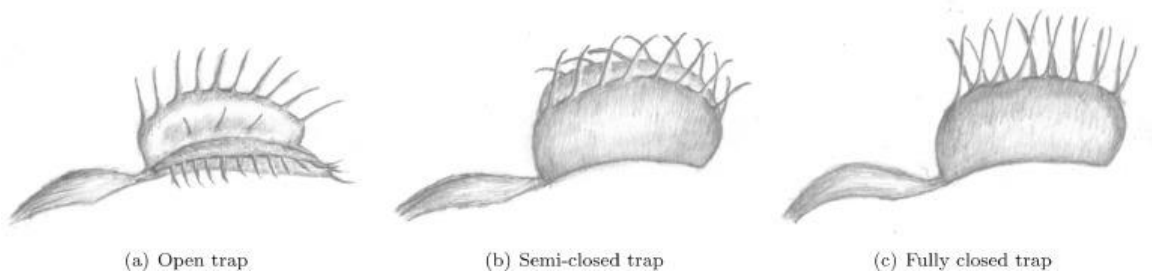

Figure 0.2: A sketch of the three trap states of the Venus flytrap, inspired by Darwin. Reprinted from [7].

These two classes of plant mechanosensation may remind neuroscientists of the two main types of mechanoreceptors in mammalian skin, the rapidly adapting (RA) and the slowly adapting (SA) [2]. In mammals these two classes of mechanoreceptors are distributed across the entire skin and can be further classified as either Type 1 or Type 2, respectively denoting either a small or large receptive field. In human tactile sensing, the four main types of mechanoreceptors are the Meissner's corpuscle (RA & Type 1), the Merkel cells (SA & Type 1), the Pacinian corpuscle (RA & Type 2), and the Ruffini endings (SA & Type 2) [2]. Like other mechanosensitive receptors, these mechanoreceptors encode their pressure information through neural spiking patterns [8]. RA receptors respond to dynamic stimuli, evoking spikes only during transitions or changes in pressure; contrarily, SA receptors respond to static stimuli, and proportionally change their firing rate with change in stimulus intensity [8] (Figure 0.3).

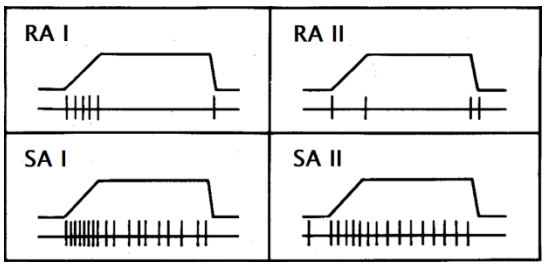

Figure 0.3: Spike trains in response to a tactile stimulus from the different types of mechanoreceptors. Reprinted from [8].

Due to their dynamic nature, RA receptors are important for large mammals, with large skins, because of their natural compression of tactile data [9]. By only responding to changes in pressure, RA receptors drastically compress static data into just two events – the beginning of the stimulus and the end. Because of this highly dynamic response, these RA receptors are essential for the discrimination of complex textures with dense spatial features [10]. When the human fingers palpate (move/slide) over textured surfaces, RA mechanoreceptors may be activated at rates up to 1000 Hz [11]. This fast dynamic response, coupled with the high-density of mechanoreceptors in the human fingertips (241 units/cm^2), enables humans to have remarkable texture discrimination capabilities [12]. For example, the human fingertips have been shown to discriminate textures with 13nm features [13] and have also been shown to be sensitive enough to distinguish surfaces that differ by only a single layer of molecules [14].

Replicating these sensing capabilities artificially is a major goal of biomedical engineering and sensor design. And although achieving human-like sensing remains elusive, in the past 40 years researchers have developed a variety of tactile sensing arrays that can record pressure, force, and vibration across large areas like the skin. These tactile

sensing arrays have been developed through many different architectures and are reviewed in chapter 1.

The rest of the thesis is organized into four additional chapters and aims to demonstrate how frequency multiplexing may be used to improve on the state of the art of current tactile sensor arrays and bring us closer to achieving human-like sensing. Thus, Chapter 2 reviews and discusses the use of frequency multiplexing in the context of increasing the scalability of current tactile sensor arrays. Chapter 3 builds off the foundations of chapter 2 and describes the design and testing of a frequency multiplexed tactile sensor array prototype. Chapter 4 describes the design and testing of a polished and scalable redesign of the frequency multiplexed sensor array using flex PCB. And lastly chapter 5 concludes the thesis with ongoing and future works.

Chapter 1

Introduction

1.1 Artificial Tactile Sensing Arrays

Artificial tactile sensing arrays (TSAs) are used to provide robotic devices with a 'sense of touch' [15]. These sensor arrays are critical in many industrial and clinical applications. For example, tactile sensor arrays have been used to develop electronic skins (e-skins) that help provide sensory feedback to amputees [16]. This chapter discusses state-of-the-art-tactile sensor arrays, how they are readout, and what their limitations are.

1.1.1 Review

TSAs have been in research since 1983, when they were developed for industrial parts handling [17]. Since then, TSAs have been developed using all sensing principles (capacitive, piezoresistive, optical, etc.). These different sensing principles and how they have been applied to develop tactile sensor arrays are reviewed in the Appendix.

For readout, TSAs typically adopt a row-column multiplexed readout scheme to reduce the number of necessary wires [18]. Row-column multiplexing requires an $m + n$ number of wires, where m and n represent the number of rows and columns respectively. This readout scheme is commonly known as time-division multiple access (TDMA) or raster scanning [19].

However, the literature shows that few raster-scanned tactile sensor arrays have many sensing elements as well as high spatiotemporal resolution. This points to the tradeoff between spatial and temporal resolution in raster-scanned systems. Because the scanning speed is fixed, as the number of sensing elements increases (spatial resolution increases), the necessary scanning time increases as well. This increase in scanning time lowers the temporal resolution.

Despite this tradeoff, some reported tactile sensor arrays have been large, dense, and fast. One example is the kilohertz kilotaxel sensor array developed by Lee et al [20]. This sensor array uses event-based encoding and a series of timers to achieve a 5.2 kHz sampling rate with 4096 sensing elements. Moreover, kilohertz spatiotemporal resolution has been shown to be critical for the discrimination of complex texture [11]. For example, the response from a population of mechanoreceptors in the skin has patterns with temporal precision of up to 0.8 msec [21]. This precision provides a rich representation of contact forces, and enables the rapid approximation of features like magnitude, curvature, and direction [21].

1.1.2 Readout

Almost all tactile sensing arrays (regardless of their sensing principle) are interfaced using time-divisional multiple access (TDMA) [22]. TDMA, or raster scanning, involves individually addressing each tactile sensing 'pixel', or taxel, in the sensing matrix one at a time before moving on to the next taxel [19]. A typical readout circuit diagram for TDMA-based TSA is shown below in Figure 1.1.

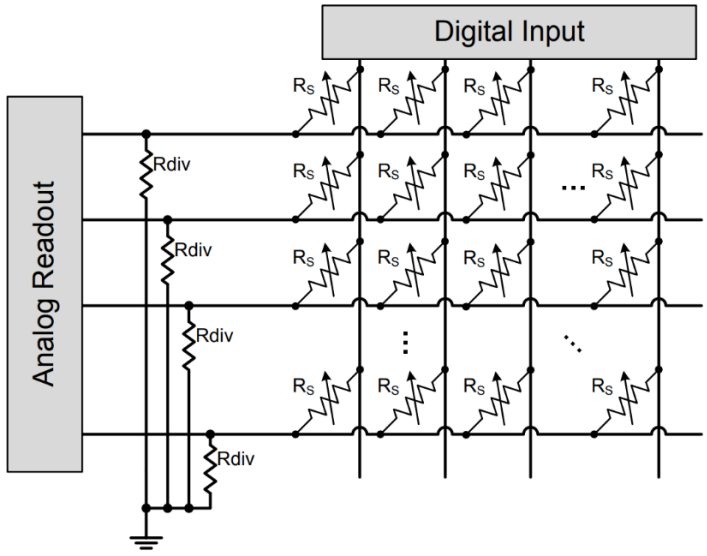

Figure 1.1: Sensor readout circuit diagram. Each row in the sensor matrix is an analog readout trace, and each column is a digital input trace. The diagonal connections represent piezoresistive material. To readout the array, digital inputs are incrementally set to 5V and the voltage values at the different analog readout traces are readout. Reprinted from [19].

The sensor readout procedure is typically accomplished using the following algorithm:

```
1:    for each digital input pin:
2:        set digital input to HIGH
3:        for each analog readout pin:
4:            read voltage at analog pin
```

```
5:        end
6:        set all digital pins to LOW
7:    end
```

1.1.3 Limitations

Larger sensing arrays utilizing a TDMA approach necessitate longer readout times to sample all the sensors in the array. This poses a significant problem to the scalability of state-of-the-art sensing arrays.

Due to this limitation, current tactile sensing arrays cannot be used for large area sensing with high temporal and spatial resolution. This is evident when considering attempts made to sensorize the entire hand [23], or other large areas like the entire body [24]. In the sensorized glove (STAG) developed by Sundaram et al [23], 548 sensors are used to collect pressure data across the palmar side of the hand with a sampling rate of ~7 Hz (Figure 1.2). However, while the STAG has a high spatial resolution due to its high density of sensors, its low sampling rate leads to poor temporal resolution.

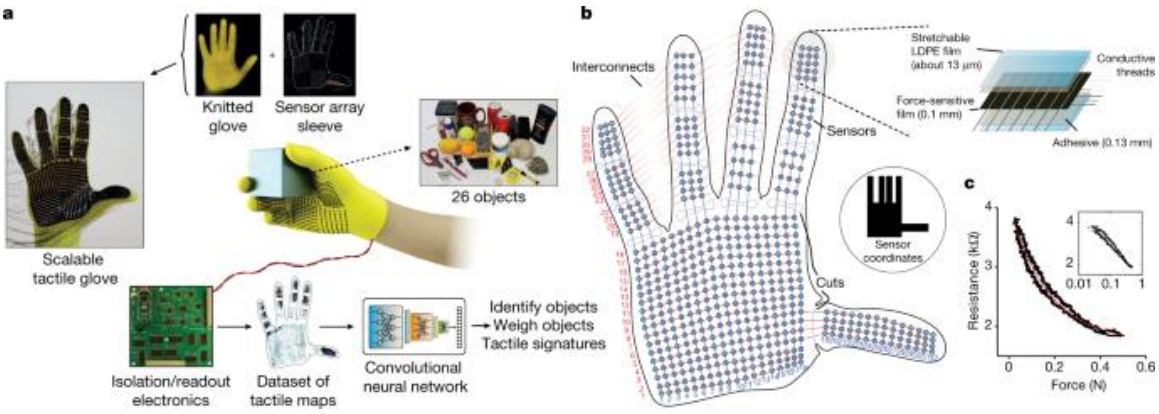

Figure 1.2: a, The STAG consists of a sensor array with 548 elements covering the entire hand, attached to a custom knit glove. An electrical readout circuit is used to acquire the normal force recorded by each sensor at approximately 7.3 fps. **b,** The design of the

STAG architecture shows the individual locations of the 548 sensors. Reprinted from [23].

Another disadvantage of TDMA and raster scanning is the large number of wires necessary for interfacing with all the sensors in the array [19]. State of the art tactile sensors that use row-column multiplexing to simplify wiring have a minimum of $m + n$ wires [19]. Even this relatively small number of wires can become unmanageable as tactile sensing arrays become large or dense with many elements.

For these reasons, an alternative to TDMA is highly desired. Particularly, an asynchronous communication method over a single wire.

1.2 Asynchronous tactile sensing e-skins

Due to the poor temporal resolution and the many wires necessary for TDMA, some groups have explored asynchronous transmission over a single wire/conductor [25,26,27]. Unlike synchronous protocols that require a clock to synchronize sensor communication, asynchronous protocols allow for sensors to communicate independently of a local clock signal [28]. This allows sensors to communicate precisely at the time of their sensing events and leads to improved temporal resolution.

Asynchronous tactile sensing schemes are also inherently biomimetic as the human skin employs asynchronous transmission natively through its mechanoreceptors [29]. This can be seen through the independent spiking behavior of each mechanoreceptor and the encoding of information through spatiotemporal patterns [29]. A discussion of three notable asynchronous tactile sensing systems is conducted below.

1.2.1 ACES

Lee et al demonstrated a novel tactile sensing system that utilizes asynchronous coding to build an artificial peripheral nervous system [27]. Their asynchronously coded electronic skin (ACES) consists of a large number of artificial mechanoreceptors that transmit asynchronously with a constant latency of 1 msec. Moreover, due to the asynchronous mode of transmission, the ACES skin has an excellent temporal resolution of just 60 ns. Additionally, due to the integrated latency, multiple signals can be combined over a single wire. This allows ACES to be highly robust to damage and highly flexible in design. The robustness to damage comes from the use of a single common conductor to transmit the artificial mechanoreceptor events. Because each sensor is independent of the others, damage to a single sensing unit allows the other sensors to maintain their functionality. This is analogous to the human body because when certain parts of the skin are bruised or damaged, the remaining mechanoreceptors are not affected and can continue their signal transduction.

To achieve these characteristics, Lee et al incorporate a microcontroller into each tactile sensing unit (taxel). This microcontroller is used to transmit a specific pulse signature that is unique to each taxel. To encode the pressure signal, Lee et al use the biomimetic approach of spike timing (Figure 1.3). Therefore, for high pressure signals, the event frequency increases, and for low pressure signals, the event frequency decreases. A downside of using this encoding scheme is that a single event is not sufficient to determine the amplitude of a pressure signal, and multiple events must occur

before the signal can be accurately reconstructed. Likewise, this encoding scheme results in light touches taking longer to register than heavier touches.

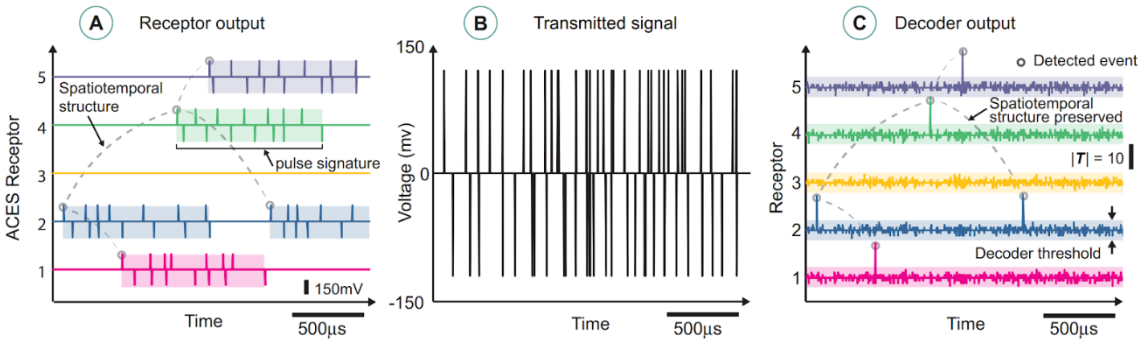

Figure 1.3: (A) ACES receptors generate tactile events with spatiotemporal structures (dashed lines) that encode the stimulation sequence. (B) Pulse signatures are combined and propagated via a single conductor. (C) Decoders match pulses in time. Reprinted from [27].

To encode pressure through event timing, each receptor incorporates a piezoresistive sensing element and some electronic components for signal conditioning. A summing op amp circuit is then used to combine all the receptor signals together from the single conductor (Figure 1.4). A notable disadvantage of this tactile sensing scheme is the complexity of each receptor, and the complexity of the algorithms used for decoding the tactile signatures presented by each receptor.

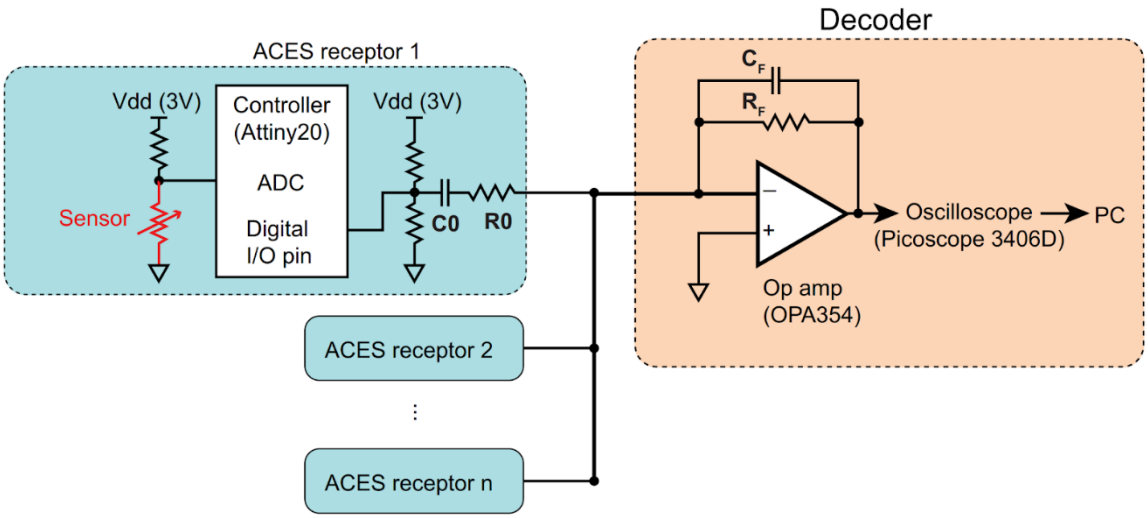

Figure 1.4: Multiple ACES receptors (blue blocks) are connected to a decoder (orange block) via a single electrical conductor. The red variable resistor represents the resistive sensors used in the current prototype. Reprinted from [27].

1.2.2 CellulARSkin

The CellulARSkin developed by Mittendorfer *et al* demonstrates an approach to realize whole-body tactile interactions using a network of multi-modal artificial skin 'cells' [25]. Each 'cell' makes up a patch of the whole CellulARSkin and patches communicate with a central reader using an event-driven state machine to transmit new data packets when sensor values deviate from sensor noise and recently transmitted samples. Each cell has an individual area of ~7cm^2, and can sense temperature, pressure, proximity to objects, and acceleration (Figure 1.5).

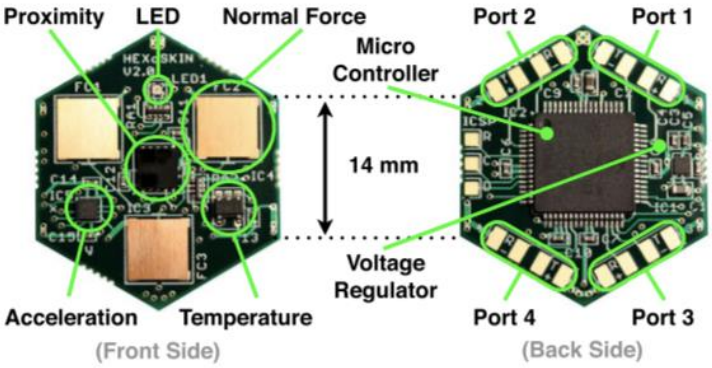

Figure 1.5: Electronics board of the modular artificial skin cell, featuring multiple sensor modalities on the front side, and local infrastructure on the back side. Reprinted from [25].

The event-driven state machine communicates with round robin packet routing, which is like raster scanning. Therefore, the CellulARSkin is not capable of supporting more than 80 simultaneous responding sensors at a refresh rate of 250 Hz [25]. Thus, to achieve human skin-like transmission speeds of 1 kHz, CellulARSkin could support a maximum of 20 simultaneously responding sensors.

A unique benefit of CellulARSkin is its capability to automatically organize itself on the fly. This allows sensors of the CellulARSkin to obtain unique IDs using a self-organized tree structure (Figure 1.6). Consequently, CellulARSkin is extremely flexible in deployment and highly reconfigurable, allowing cells to be arranged in arbitrary shapes with a dynamic method of assigning sensor IDs to each cell.

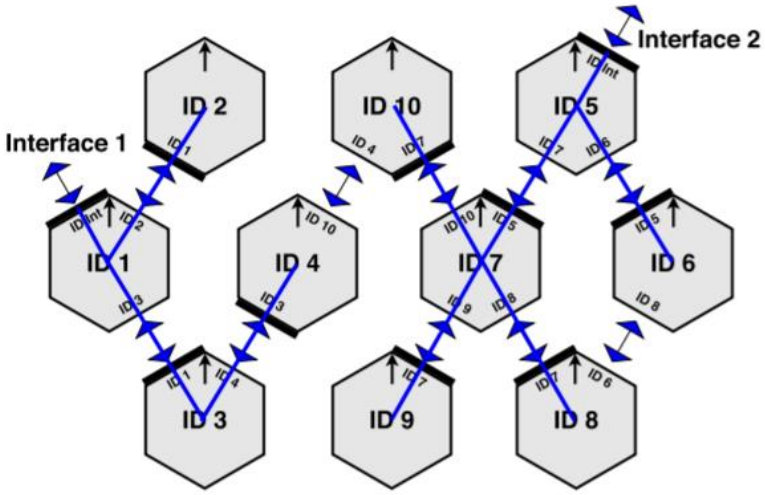

Figure 1.6: Example of the network organization in CellulARSkin. Reprinted from [25].

1.2.3 RFID Hand

Our group has also attempted to mitigate the limitations of TDMA using wireless, asynchronous methods [30]. Instead of using a single wire for signal transmission, we have proposed the use of a wireless system using RFID to transmit unique receptor IDs (analogous to the ACES pulse signature). Unlike the ACES scheme, our asynchronous RFID transmits binary pressure rather than analog, although a similar analog transmission scheme could be adopted using event timing modulation.

To transmit binary pressure data in an event-based manner, an air gap was utilized to modulate the responses of different RFID tags. By separating an RFID chip from its antenna, the RFID tag is transformed into an event-based binary pressure sensor. This was implemented by implanting the RFID chip and antenna in a silicone elastomer with a specific air gap between the antenna and chip. Because the silicone elastomer is elastic, pressure on an RFID taxel deformed the material and allowed for contact between the

RFID chip and its antenna – causing the RFID tag to transmit its ID number, and therefore the location of the pressure event (Figure 1.7).

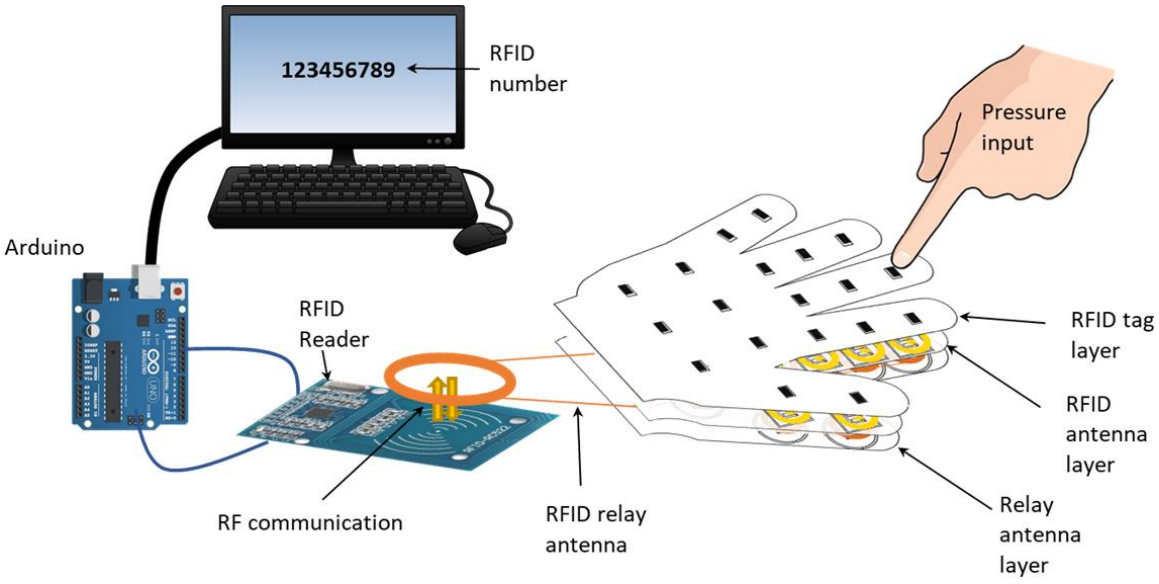

Figure 1.7: Overall system setup to power and read pressure data from the RFID Hand. An Arduino UNO is used to interface a computer with the RFID reader. A computer program records and displays which RFID taxels respond to different pressure inputs. The pressure location can be realized due to a one-to-one mapping between each tag's ID and its location in the RFID Hand. Reprinted from [30].

This RFID-based solution, which we called the RFID Hand, served as a proof of concept for how to build flexible tactile sensing arrays that are scalable to large amounts of sensors. A potential downside of the RFID Hand is that as the number of simultaneously responding taxels increases, the readout time increases as well. This is due to the anti-collision protocols that RFID readers employ when communicating with groups of RFID tags. Because the RFID reader is only capable of reading a single RFID tag at a time, when multiple tags respond they form a queue. Moreover, the queue completion time is not linear and large queues take longer to process than a linear

relationship would suggest. Still, the RFID Hand is, to the best of our knowledge, the only developed asynchronous, event-based tactile sensing scheme that can be powered and readout completely wirelessly. This makes RFID-based tactile sensors a good candidate for complex, intricate sensor designs where wiring can introduce problems. For example, RFID-based sensors can be good candidates for developing multi-layer, distributed tactile sensors. With a variety of tactile sensing elements throughout various layers, a wireless approach is desirable for facile implementation.

1.2.4 Limitations

Despite the advantages of the ACES skin, CellulARSkin, and the RFID hand, all three systems are non-optimal, and have their own unique sets of problems.

For example, the ACES architecture results in a high degree of computational complexity in the receiver, and it is also impossible for the receiver to know if a loss of a sensing event occurs [27]. Additionally, because each taxel must transmit a complex and unique pulse signature, each taxel requires a dedicated microcontroller. This is problematic for developing dense tactile sensor arrays. The smallest commercially available microcontrollers are on the order of 2mm in size [31], constraining individual taxels to be at least that large. Emulating human-like sensing will require a higher density of tactile sensors as the human fingertips have a mechanoreceptor density of 241 units/cm^2 [12]. Moreover, the ACES architecture encodes pressure data through firing rate modulation. Therefore, multiple pulse signatures must be read before realizing the sensor measurement. Likewise, the CellulARSkin also requires complex electronics inside each ‘cell’ of the skin and therefore is limited in density like the ACES receptors.

Additionally, the number of simultaneously responding sensors is relatively low because of the round-robin communication scheme. Although most human tactile interactions contain sparse tactile signals, the maximum of 20 simultaneously responding sensors is limiting for creating large sensor arrays. This also excludes the CellulARSkin from utilization in applications where simultaneous touch scenarios are common.

Unlike the ACES architecture or the CellulARSkin, the RFID Hand does not suffer from the same scalability limitations. This is because RFID research has focused on developing extremely small tags, with the smallest tags having a 0.05 x 0.05 millimeters footprint [32]. Such a small footprint could theoretically allow for a tactile sensing array with a sensor density of 400 units/cm2. However, despite the scalability of the RFID Hand, the RFID Hand has poor sensor resolution and is only designed to transmit binary values. Another limitation of the RFID Hand is that as the number of simultaneously responding taxels increases, the readout time increases as well. This limitation is common in both the RFID Hand and the CellulARSkin. When multiple tags respond concurrently, the RFID tags are put into a queue and handled one at a time. Moreover, the queue is non-linear and longer queues take much longer to resolve. Lastly the RFID Hand has a relatively complex readout antenna. This complex design is constructed to promote efficient communication with all the tags. However, the authors argue that it is possible to reduce the complexity of the antenna.

Chapter 2

Spatial frequency encoding for scalable e-skins

Spatial frequency encoding is a type of frequency multiplexing that encodes different spatial locations as different frequencies sinusoids [33]. This encoding is particularly useful for applications requiring single conductor or single wire signal transmission due to the orthogonality of different frequencies [34]. Due to this orthogonality multiple signals can be combined over one conductor without destructive interference. Thus, frequency encoding is most used in wireless communication [35]. For example, in radio communication different radio signals are confined to specific frequencies and all the signals simultaneously transmit through the air. Tones/pitches in music are also frequency encoded, with higher frequency sounds having a higher pitch.

Historically, spatial frequency encoding has been used in magnetic resonance imaging (MRI) and nuclear magnetic resonance (NMR) imaging to encode spatial

position as specific frequencies (Figure 2.1) [36]. For brain imaging, spatial frequency encoding allows for non-invasive 3-dimensional imaging. By representing different slices/depths as a different frequency, the entire brain can be imaged, and all the slices can be resolved through spectral analysis [36].

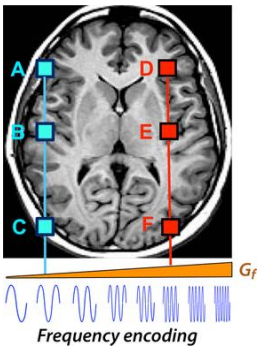

Figure 2.1: A linearly increasing frequency-encoding gradient (G_f) applied along the horizontal (x-) axis. Pixels A, B, and C all resonate at the same lower frequency; D, E and F at the same higher frequency. Reprinted from [37].

2.1 Theory

From a telecommunications perspective, spatial frequency encoding is a form of frequency division multiplexing (FDMA) [35]. FDMA has been used in wireless communication since 1983 and was used in the first-generation of cell phones [38]. FDMA divides the available channel bandwidth into many unique frequency channels [35]. Each transmitter has a dedicated channel and thus all users can communicate simultaneously.

The simultaneous communication capability of FDMA can be understood by examining the combinations of different frequency signals in simulation. For example, the plot below shows how signals with different frequencies are added together, and how

the resulting waveform can be resolved into its constituent components using a Fourier transform.

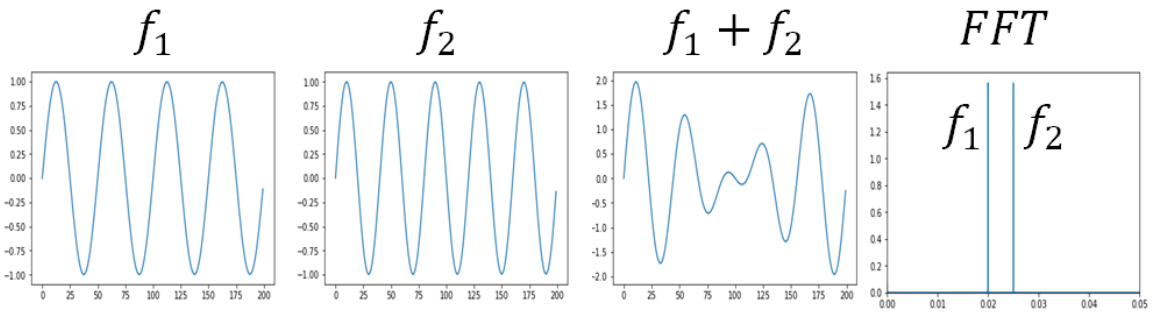

Figure 2.2: Orthogonal frequency combination and spectral analysis.

An important aspect of frequency encoding is the use of guard bands to separate frequencies [35]. Because the FFT algorithm uses frequency bins rather than a continuum of frequencies [39], and the sampling time is fixed, it is important to ensure adequate band spacing between different frequencies. This is achieved by using guard bands between signal carrying bands/frequencies [35]. These bands do not carry any signal and are used to ensure accurate peak detection in the frequency analysis.

Because of the substantial bandwidth of the radio frequency band (kHz to THz+), spatial frequency encoding is useful for applications involving many sensing elements. The total number of possible frequencies that can be used for encoding depends on the desired sampling rate of the tactile sensor array and the sampling rate of the ADC used to readout the sensor array. By Nyquist's theorem, to accurately measure a signal it must be sampled over twice as fast as its maximum frequency component [40]. This implies that the maximum encoding frequency is $\frac{ADC_{freq}}{2}$. The minimum encoding frequency is

determined by the desired sampling rate for the tactile sensor array. For robust FFT detection, the minimum frequency separation should equal the sampling rate. Thus, the channel number is determined by the following formula:

$$Channel\ Number = \frac{\frac{ADC_f}{2} - sampling\ rate}{sampling\ rate}$$

For example, a tactile sensing system with a 1kHz sampling rate and a 1 GHz ADC will have: (500MHz - 1kHz)/1kHz = 499.999 MHz / 1kHz = 499.999 k = 499,999 possible channels. Moreover, this total channel number is a lower bound as the frequency spacing can be decreased. For example, it has been demonstrated that the minimum frequency separation can be 1/2T rather than 1/T [41]. This doubles the possible channel count to almost 1 million.

When calculating the FFT it is important to use frequency bins at least twice as fast as the specified channel spacing [41]. This ensures that there is at least one guard band for each transmission band. By allocating guard bands in the FFT, the peaks in the spectrograph can be reliably detected/discriminated.

The implementation of spatial frequency encoding systems is carried out in four steps: carrier wave generations, wave modulation, signal integration, and decoding. These steps are reviewed in the Appendix.

2.2 Dual-Tone Multi-Frequency Encoding

Rather than using a single-tone frequency encoding as described above, in this work dual-tone multi-frequency encoding (DTMF) is used. Instead of assigning a single

frequency to each sensing element, each row and column of the sensor array are assigned a unique frequency [42]. Thus, the intersection of a row and column create a tuple of frequencies, like an x-y coordinate system. Historically, DTMF has been commonly used in telephone keypads (Figure 2.3) and the activated dual tones are audible when pressing a button on a phone [42]. Although these touch-tone keypads are binary touch sensors, piezoresistive materials can be used to convert the binary touch sensor into an analog tactile sensor array.

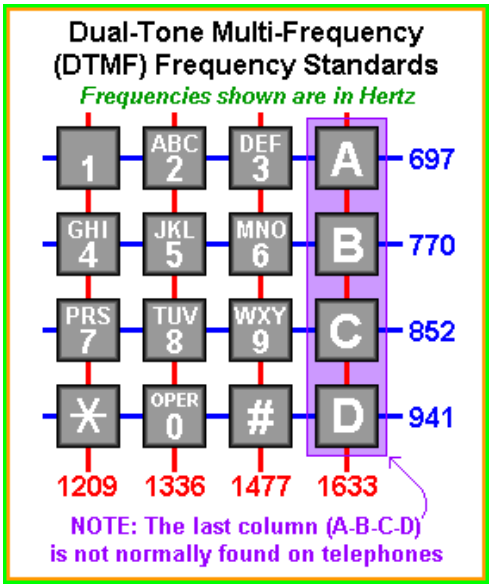

Figure 2.3: DTMF touch-tone number pad. Reprinted from [43].

DTMF has two primary advantages over conventional single tone encoding systems for the development of sensor arrays: innate data compression, and the enabling of electronics-free taxels.

Because each row and column of a DTMF sensor array is assigned a unique frequency, the number of frequencies for a $M * N$ sensor array is $M + N$. For small tactile

sensor arrays this scaling is not significant, but as the sensor array grows this relationship significantly reduces the number of frequencies required for analysis. For example, to readout a $1000 * 1000$ sensor array with 1,000,000 sensing units only 2,000 frequencies need to be analyzed. This makes DTMF very promising for real-time sensing applications in large sensor arrays with many sensors.

Electronics-free taxels are also enabled by the dual-tone design. Because a taxel is defined as an intersection of a row and column in a DTMF sensor array, each taxel does not require any frequency generating circuitry. This is especially attractive for the development of tactile sensor arrays because it allows for a high-density design, high flexibility, and the utilization of materials not standard in conventional circuit design. For example, fabric-based e-textile materials can be used to replace the rows/columns of a sensor array to develop a soft, flexible, and stretchable sensor array.

A single tone system could also be designed to not require any frequency generating circuitry per taxel; however, it would require significantly more wires to interface with each taxel as the number of wires would scale with the number of sensors rather than the number of rows/columns.

Chapter 3

Neuroskin 1

The following chapter was presented at the 10th International IEEE/EMBS Conference on Neural Engineering (NER) and was published in the conference proceedings [44].

Neuroskin 1 is a fabric-based prototype of a 3x3 spatial frequency encoded tactile sensor array. The fabric-based e-textile materials allowed the sensor to be highly flexible and conformable. To test the performance of Neuroskin 1, a texture discrimination task[1] was performed by mounting Neuroskin 1 onto the fingertip of a soft robotic finger. The sensorized soft robotic finger was then attached to a UR5 robotic arm and a library of

[1] Texture was chosen as a model task because of the complex spatiotemporal nature of texture palpation. Because applied pressures change spatially and temporally during texture palpation, accurate texture discrimination requires a tactile sensor with both a high spatial resolution and a high temporal resolution.

different texture plates were palpated. Across the different texture plates, Neuroskin 1 achieved an overall texture discrimination accuracy of ~87%. An overview of the texture discrimination task is shown below in Figure 3.1.

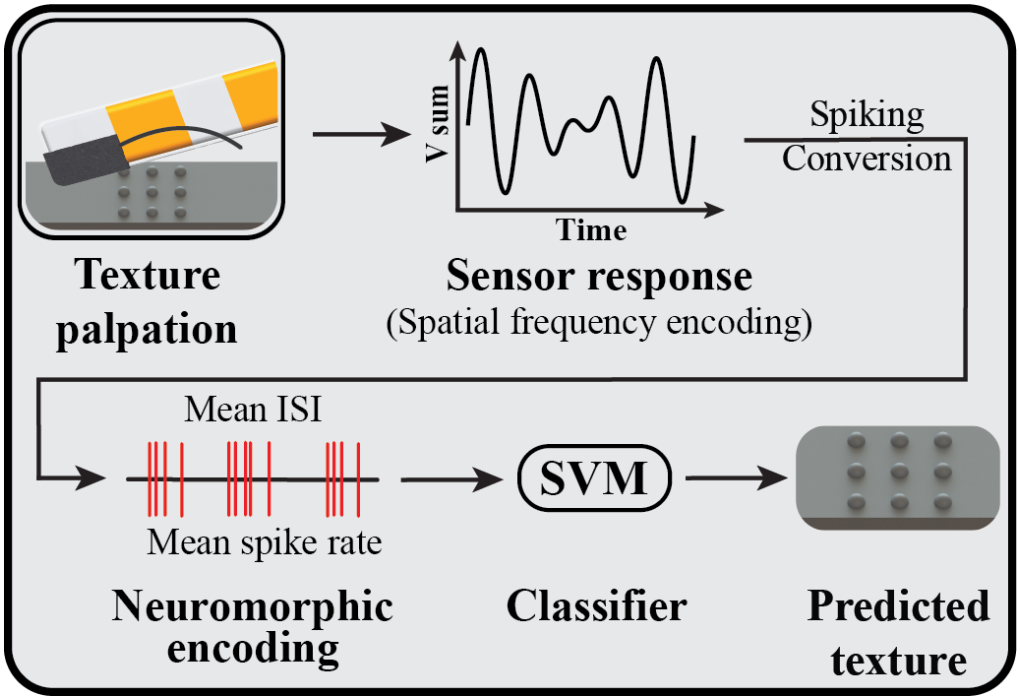

Figure 3.1: Diagram showing the overview of the texture discrimination. Reprinted from [44].

Neuroskin 1 comprises two proof-of-concept prototypes that were developed using fabric-based e-textile materials with amplitude modulated sinusoidal carrier waves. The prototype devices used DTMF encoding to simplify fabrication and allow for a denser sensor array with fewer wires. Rather than assigning a unique frequency to each sensor, the DTMF encoding assigned a unique frequency to each row and column of the sensor array. Thus, each taxel of the sensor array was represented as a combination of two frequencies, like an x-y coordinate system (Figure 3.2). A piezoresistive layer was used

to amplitude modulate which coordinates are transmitted to the receiver; and spectral analysis is used on the receiving side to decode which locations were activated on the sensing matrix with what pressure.

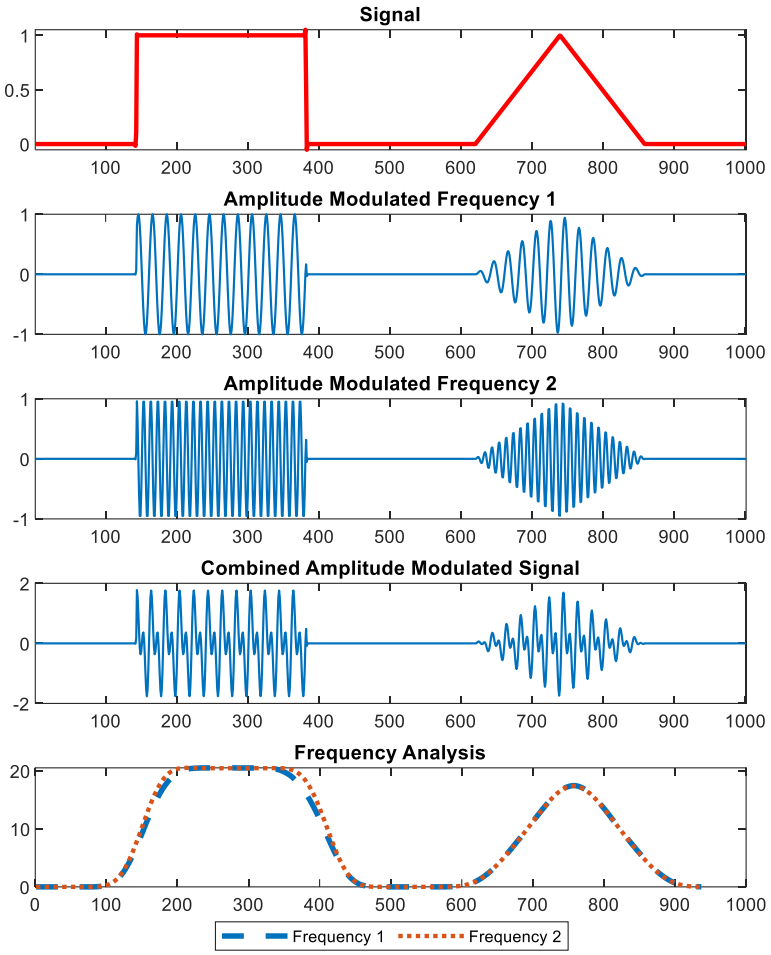

Figure 3.2: Diagram showing tactile dual-tone multi-frequency encoding. A single taxel is associated with 2 carrier frequencies, and a piezoresistive layer amplitude modulates these carrier waves to combine onto a single conductor. Frequency analysis is performed on the combined signal to reconstruct the applied pressure.

Because of the simultaneous and asynchronous behavior of the DTMF-based tactile sensing system, Neuroskin 1 mimics how mechanoreceptors transduce pressure signals in the skin (Figure 3.3).

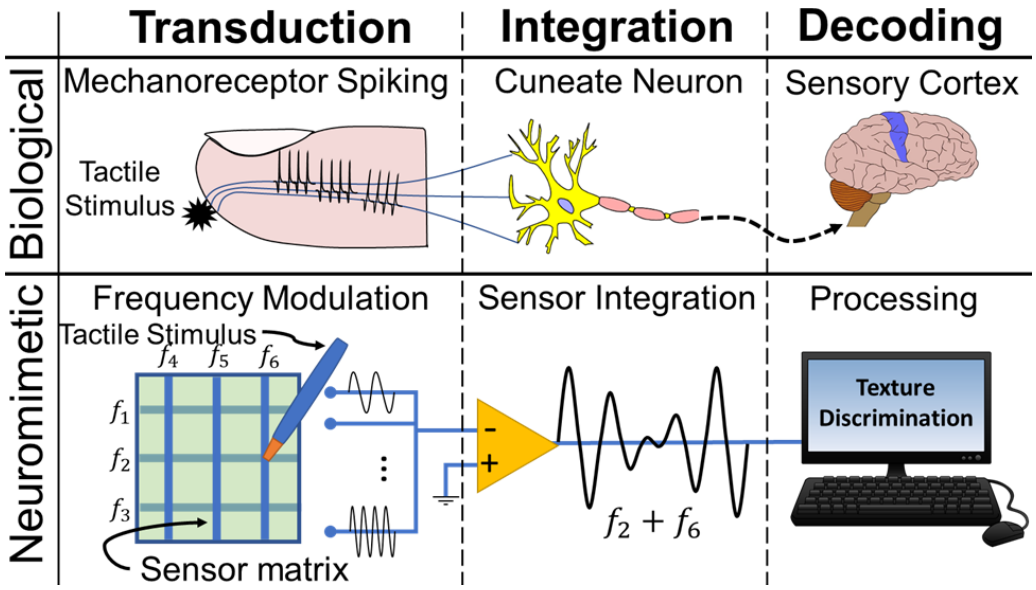

Figure 3.3: Schematic describing neuromimetic approach of spatial frequency encoding. The top row represents the biological pathway of tactile sensation, and the bottom row describes the investigated neuromimetic approach. Reprinted from [44].

3.1 Sensor array fabrication

The tactile sensor array was fabricated using e-textile materials to be flexible and conformable. This approach has been demonstrated before in our group's previous papers [45,46]. However, to achieve spatial frequency encoding, the typical fabrication structure was slightly altered. An overview of the fabrication of both prototypes is described in Figure 3.4. The primary difference between the new fabrication structure is the introduction of a large piece of conductive fabric to transmit the different frequency signals across a single common wire. Figure 3.3b shows a second fabricated design that operates over two conductors rather than one. Because the design presented here uses DTMF, it is possible to read out the coordinates over two separate conductors (for x and y).

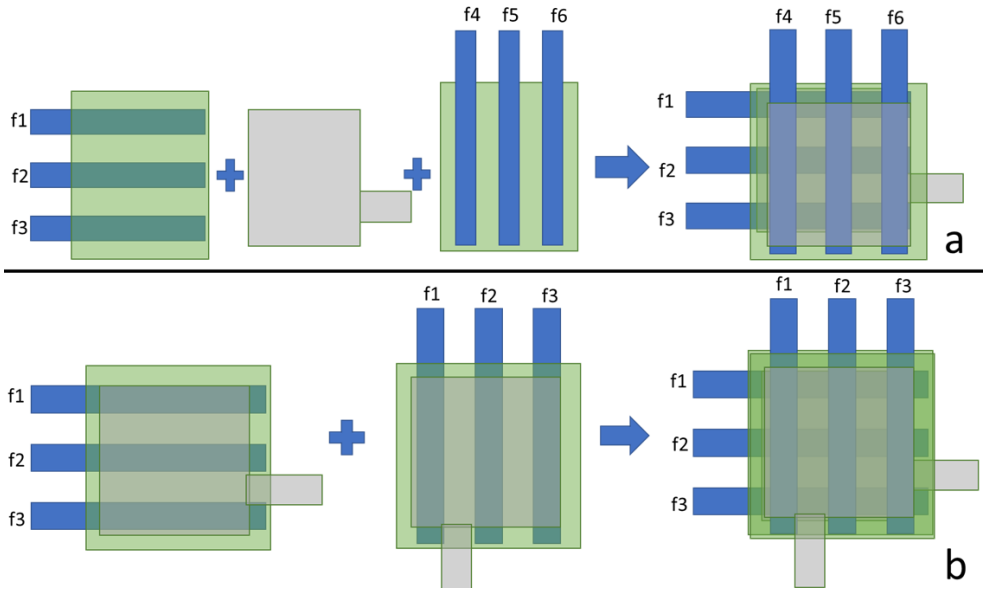

Figure 3.4: Fabrication schematic of the two spatial frequency encoded prototype devices. Green represents piezoresistive fabric (Stretchy Piezo LTT-SLPA-150k, Eeonyx), blue represents conductive fabric (Silver plated mesh, LessEMF), and gray also represents conductive fabric. Transparency in the colors represents overlapped elements with darker elements appearing on top of lighter ones. **a.** Utilizes a single common conductive layer, and **b.** utilizes two common conductive layers (one for row frequencies and one for column frequencies).

3.2 Sensor readout and spectral analysis

Spectral analysis is used to resolve which frequencies are present in the measured signal and with what amplitude they are present. A Fourier transform is used to convert the signal from the time domain into the frequency domain. The peaks present in the transformed signal are then analyzed to resolve the amplitudes of the different frequency signals. The general encoding and decoding scheme are demonstrated below in Figure 3.5. As different spatial locations in the sensor matrix are activated, different frequency sinusoids are amplitude modulated and summed into a combined voltage. The spectrum

of this combined voltage is then analyzed to resolve the frequencies, and their corresponding amplitudes, to determine the pressure signal applied on the sensor array.

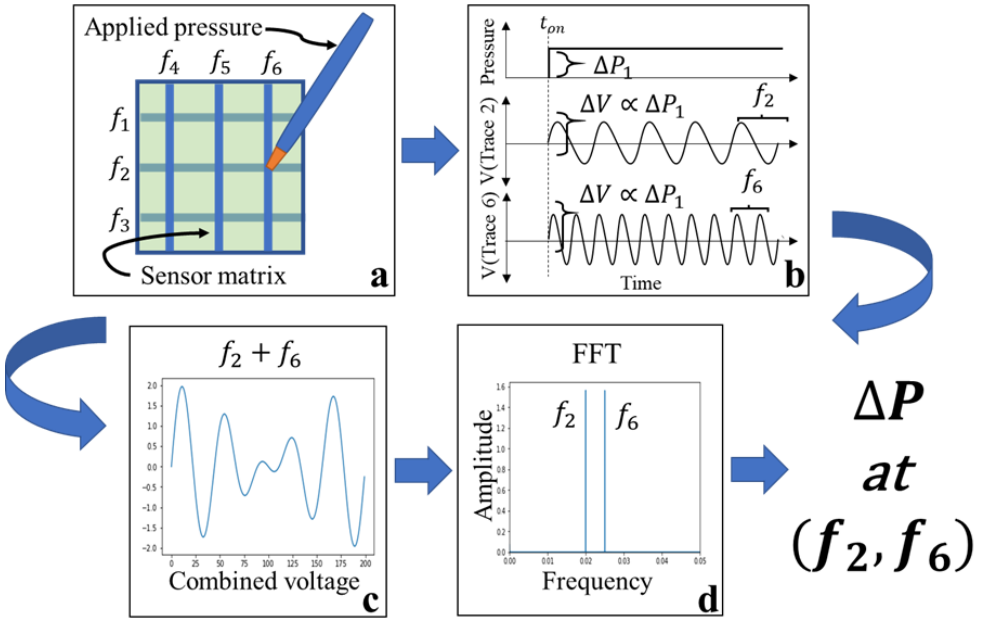

Figure 3.5: Flow chart showing spatial frequency encoding and decoding for a coordinate-based spatial frequency encoded tactile sensing matrix. (a) shows applied pressure to the taxel (f2, f6), (b) shows the different frequency voltage responses to be summed on the single conductor. (c) shows the combined voltage, and (d) shows the resolved frequencies in the FFT. Reprinted from [44].

We demonstrate the use of the spatial frequency encoded sensor in a texture discrimination task. Thus, we calculate the short-time Fourier transform (STFT) in windows of length 1500 (~100msec). This number was picked empirically by trying different window values and measuring the relative power of the spectrum. An example STFT plot for the fabricated sensor is shown below (Figure 3.6). This plot represents an STFT calculated after sequentially indenting the nine different taxels of the tactile sensor array. Notably, the plot shows how an indentation of each taxel results in two dominant

frequencies in the STFT. This combination of frequencies is used to resolve the location of the applied pressure.

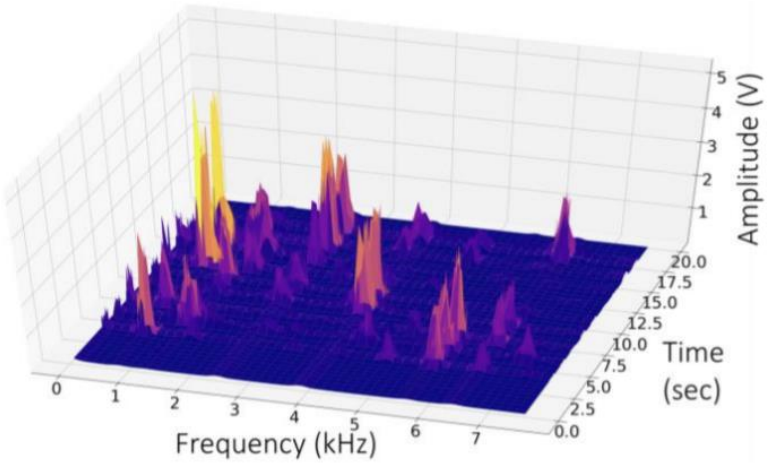

Figure 3.6: Generated STFT plot of frequency vs time vs amplitude in response to sequentially indenting the nine different taxels of the tactile sensor array. As time increases, pressure is applied to different taxels and is represented in the STFT as a peak at two different frequencies. Reprinted from [44].

To convert the spectral data into different taxel values, the following algorithm was used. In the algorithm, 'amp' refers to the amplitude of the frequencies (f1, …, f6) measured by the STFT.

$$Taxel\ 1 = amp(f_1) * amp(f_4)$$
$$Taxel\ 2 = amp(f_1) * amp(f_5)$$
$$\dots$$
$$Taxel\ 9 = amp(f_3) * amp(f_6)$$

Following this algorithm, nine taxel values were calculated for each window in the STFT based on the amplitudes of the six carrier frequencies present in that time window.

3.3 Experimental procedure

To test the spatial frequency encoded sensor, a texture discrimination task was performed using an experimental procedure from a previous study [47]. The sensor was attached to a soft biomimetic fingertip, which was mounted on a UR5 Robot arm (Universal Robotics). The pneumatically actuated soft biomimetic finger had an input pressure of 15 psi, which resulted in a 30° angle of flexion. The finger then palpated across a library of 10 3D printed textured plates (Figure 3.7), for a total of 38 trials per texture. The signal was measured on the single common conductor and saved for offline analysis. After obtaining the data, the spectral content was examined as described in section 3.2, and the taxel values were resolved. To further emulate the firing pattern of biological mechanoreceptors, taxel values from each taxel were converted into neuromorphic spike trains using the Izhikevich neuron model [48]. This neuromorphic encoding allows for the extraction of temporal spike-based features such as inter-spike-interval (ISI) that reduce the dimensionality of the data and add robustness against trial-to-trial time misalignments These spike-based features were then classified using a support vector machine (SVM).

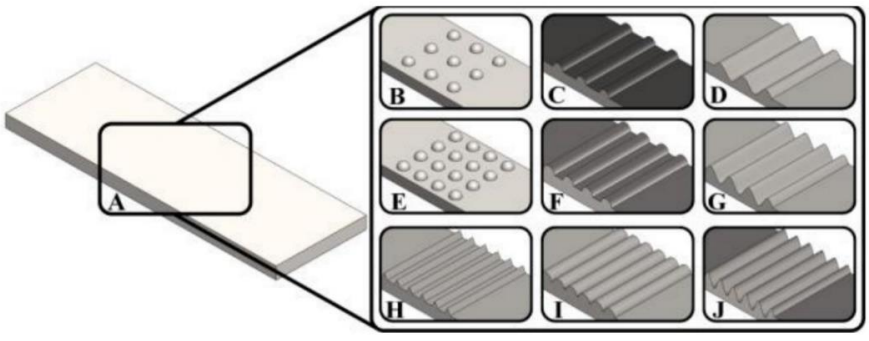

Figure 3.7: 3D printed textured plates used in texture discrimination task. Reprinted from [44].

As a comparison, the texture discrimination task was also performed on a 3x3 TDMA sensor constructed from the same materials as the spatial frequency encoded sensor. In the TDMA sensor, there are 3 input wires and 3 common wires, and a sampling rate of 100 Hz.

3.4 Results

The sensor had a spatial resolution of 4 mm^2, based on the width of the conductive fabric, and a temporal resolution of 1.75 kHz, which was limited by the minimum carrier wave frequency and the ADC sampling rate. For reliable FFT detection, at least one period is required to be present in a sampling window; thus, the minimum frequency carrier wave determines the sampling window size and limits the temporal resolution. However, for reliability in the texture discrimination experiment, ~100msec STFT time windows were used rather than the theoretical minimum of 0.6 msec.

In the texture discrimination task, the spatial frequency encoded sensor achieved an accuracy of 86.58%. The TDMA tactile sensor achieved an accuracy of 98.95% over the same texture library. The classifier metrics of the texture discrimination task with a comparison between the spatial frequency sensor and the TDMA sensor are presented in Table 3.1 below.

Table 3.1: Texture discrimination classifier metrics.

	Spatial Freq. Sensor	TDMA Sensor
Accuracy	0.8658	0.9895
Error rate	0.1342	0.0105
Sensitivity	0.9737	1
Specificity	0.9912	1
Precision	0.925	1
Negative Predictive Value	0.9971	1

An example spectrogram for one of the samples used in the texture discrimination task is shown below in Figure 3.8. As evident from the graph, only certain frequencies have strong responses for this texture sample. Over time as the finger palpates over the texture, the amplitudes corresponding to different frequencies vary, suggesting changes in pressure on the sensor array analogous to the texture's profile.

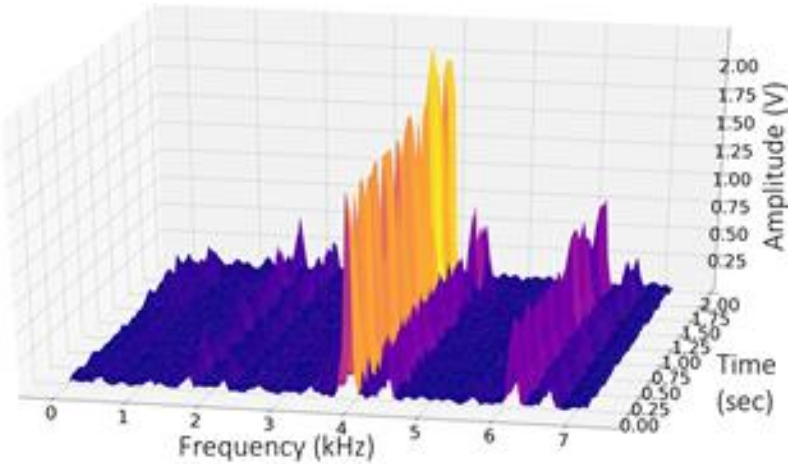

Figure 3.8: Generated STFT plot of frequency vs time vs amplitude in response to sequentially indenting the nine different taxels of the tactile sensor array presented in Figure 3.4a. As time increases, pressure is applied to different taxels and is represented in the STFT as a peak at two different frequencies. Reprinted from [44].

3.5 Discussion

In the texture palpation experiment, the spatial frequency encoded sensor array had comparable performance to the TDMA sensor array, but with slightly lower accuracy. However, because this is the first presentation of spatial frequency encoding in the application of tactile sensor arrays, it is possible that the decoding algorithms (i.e., STFT) can be further optimized to increase classification accuracy.

Overall, the neuromimetic spatial frequency encoded tactile sensor system presented here had many advantages over the current raster-scanned state-of-the-art. Notably, these advantages include single-wire signal transduction and asynchronous sensor responses. Thus, the only potential latency in the sensing system is introduced by the sampling rate of the ADC. The prototype sensor developed here had 6 wires coming into the device because the phase shift oscillator circuits were built on an off-the-sensor circuit board. In future works, these circuits can be miniaturized to fit on the perimeter of the tactile sensor array through fPCB development (see chapter 4). By placing the oscillators on the perimeter of the sensor, only three total wires could be necessary: one for power/Vcc, one for ground, and one for signal transmission. This is a significant reduction since TDMA sensor arrays require $m + n$ number of wires.

The matrix design and DTMF encoding strategy minimized the necessary oscillators to $m + n$ rather than $m * n$ but had some inherent limitations as well. For example, because there are only six frequencies present, and nine possible taxels to be activated, if multiple taxels are activated along the same row or column simultaneously, there is some averaging in the response. This can be understood because of the additive

model where the amplitude of a frequency depends on the total pressure applied to a certain row or column. To mitigate this issue, $m * n$ carrier frequencies can be used. This would ensure that each taxel has its own independent frequency and eliminate the averaging issue. However, this approach requires integrating an oscillator into each taxel of the sensor array and can pose limitations for creating sensor arrays with a very high density.

Ultimately, the bandwidth of a spatial frequency encoded system is limited by the ADC and the desired resolution of the application. For reliable FFT detection, it is generally required that at least one period of a signal is present in the time window investigated. This implies that depending on the desired resolution of the system, the lowest possible frequency used for encoding must equal the desired resolution. The maximum frequency that can be used for encoding is limited by the ADC frequency and Nyquist sampling. Furthermore, the minimum channel spacing is equal to the desired resolution.

3.6 Conclusion

The developed neuromimetic spatial frequency encoded tactile sensor array achieved a texture classification accuracy of 86.58% and had comparable performance to the state-of-the-art TDMA-based tactile sensor array. Moreover, the developed prototype had a higher sampling rate than the TDMA-based tactile sensor array and transduced sensor data over a single wire rather than a multitude of wires. The method of spatial frequency encoding enables no latency between sensor responses and is promising for discriminating textures with a high degree of spatiotemporal complexity. Overall, the

developed neuromimetic spatial frequency encoded system demonstrates how future tactile sensing systems and e-skins can be fabricated to be numerous and dense, while retaining excellent temporal resolution and signal transduction over a single wire.

Chapter 4

Neuroskin 2

Neuroskin 2 builds directly on Neuroskin 1 by utilizing a flexible-PCB to create a highly scalable design. Neuroskin 2 significantly simplifies the wiring of its predecessor by compacting the carrier wave generating circuitry to the perimeter of the sensor array. Neuroskin 2 requires only 4 connection wires, 3 for power and 1 for signal, regardless of the number of sensing elements. Like Neuroskin 1, the ability of Neuroskin 2 is demonstrated through a texture discrimination task where Neuroskin 2 achieved an average discrimination accuracy of 76% on a library of 3D printed textures. Neuroskin 2 is also briefly characterized by analyzing the force response of the sensing elements.

4.1 Design and Fabrication

Neuroskin 2 is developed as a 3x3 sensor array using DTMF, with 6 carrier frequencies for 9 sensing taxels (Figure 4.1). Op amp-based phase shift oscillator circuits are used to generate the different carrier waves of the sensor array and 0805 size resistors and capacitors are used in the design. A summing amplifier is used to combine the

mixed-frequency signal onto a single wire without taxel-to-taxel interference. The sensor is developed on a fPCB and was designed in KiCAD [49] and produced by PCBWay [50]. All fPCB circuit components were soldered by hand at JHU.

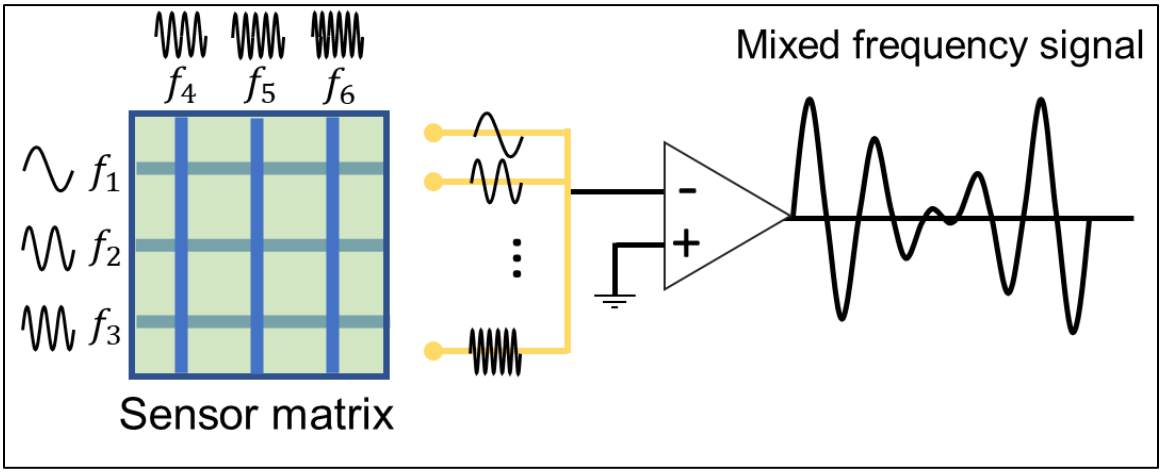

Figure 4.1: Drawing of the sensor principle of Neuroskin 2. Each row and column are assigned a unique frequency and a piezoresistive fabric amplitude modulates tuples of frequencies at the location of pressure. The transmitted frequencies are amplified by a summing amplifier onto a single wire that goes to a microcontroller for analysis.

The phase shift oscillator circuit was arranged in a compact design as shown below (Figure 4.2). Resistor and capacitor values were chosen by following the formula:

$$f_{osc} = \frac{1}{2\pi RC\sqrt{6}}$$

The temporal resolution of the sensor array was designed to be 1 msec to mimic the temporal resolution of human mechanoreceptors. Thus, the resistors and capacitor values were chosen accordingly to create 6 different frequencies, starting at a minimum of 1 kHz with a minimum spacing of 1 kHz. This was done to ensure that spectral analysis could accurately detect any of the carrier frequencies in a 1 msec time window, and that in that

time window all frequencies had a difference of at least 1 period. The resulting frequencies used in the sensor array were calculated to be: 1.9 kHz, 3.3 kHz, 5 kHz, 7.14 kHz, 8.3 kHz, and 10 kHz.

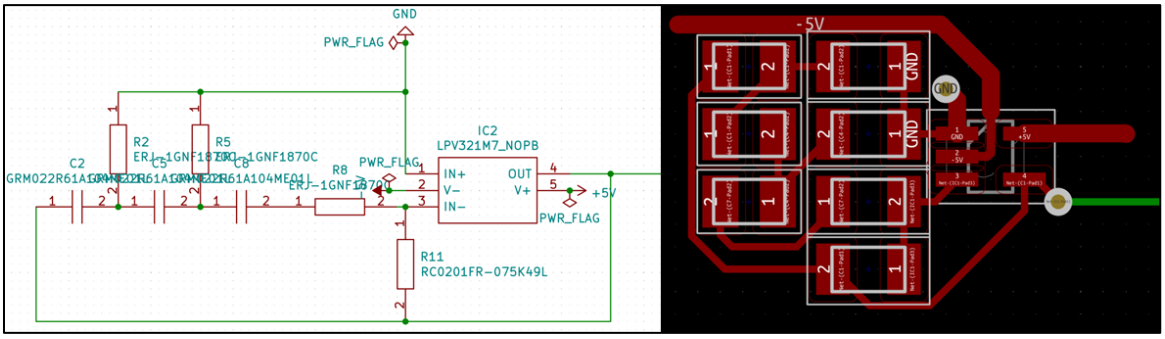

Figure 4.2: PCB layout of the phase shift oscillator circuits present at each row and column. Left shows schematic organization from KiCAD, and right shows the organized components for PCB population.

The sensor array was developed in a 5-layer design (Figure 4.5), with 3 fPCB boards in each sensor. The top fPCB contained the row elements, the bottom fPCB contained the column elements, and a middle fPCB contained a large copper square that allowed all the signals to combine to a single conductor. All row traces and column traces were designed as bare copper to ensure high conductivity. The front and back of the top layer is shown below in Figure 4.3 in a 3D view. The bottom layer is identical to the top layer but with a 90-degree rotation and an inversion of the traces on front side and components on the back side.

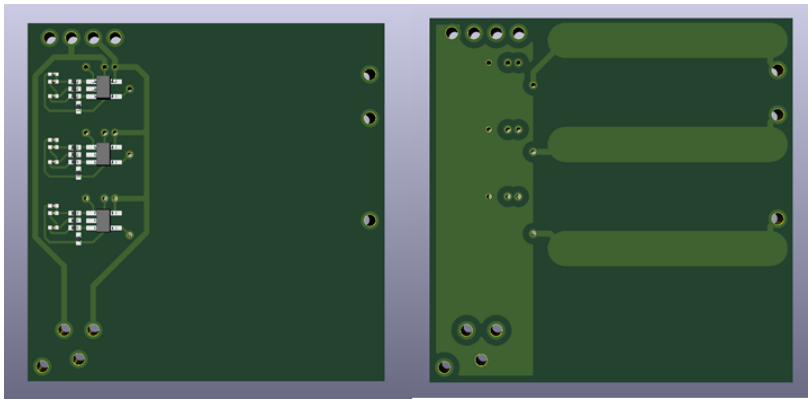

Figure 4.3: 3D view of Neuroskin 2 top layer. 3D view shows rigid PCB, although prototype is developed with a polyimide substrate. Left image shows the front of the sensor with arranged phase shift oscillator circuits and centralized power lines. Right image shows the back side of the sensor with conductive traces that serve as the conductive rows in the sensor array.

The produced fPCB boards are shown below in Figure 4.4. They are fabricated with a polyimide substrate and are highly flexible. The fPCB boards measure 36.195mm x 34.29mm with a sensing area of 4cm^2. The fPCB is designed so all four connections are routed to one corner of the board. This allows for a compact soldering of four thin wires (like ribbon cable) to the sensor array. After stacking the 3 layers on top of each other, solder is used to connect the layers electrically through the 4 through holes on the corner of the board.

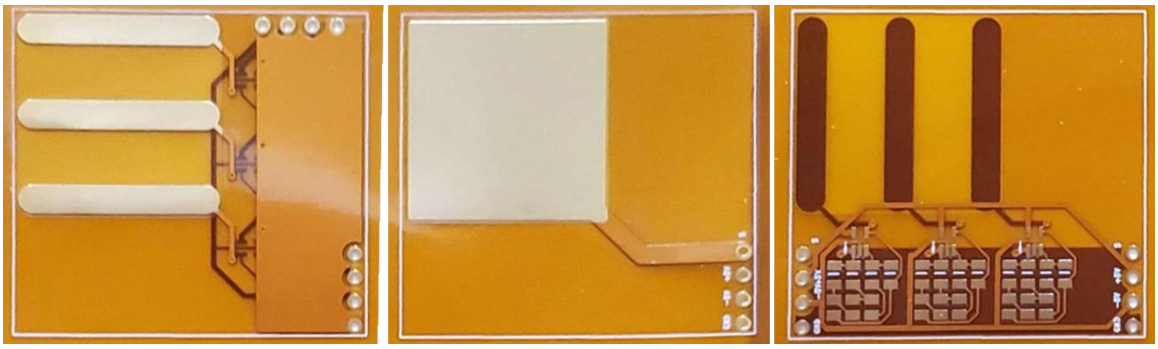

Figure 4.4: Images of the produced fPCB boards. Left image shows top layer containing the conductive row elements, middle image shows the summation layer where

frequencies are combined, and the right image shows bottom layer containing the conductive column elements.

The layers are then populated and sandwiched together with two layers of piezoresistive fabric (Eeonyx) to form a 5-layer sensor (Figure 4.5). The piezoresistive fabric is secured in place with a small amount of Kapton tape.

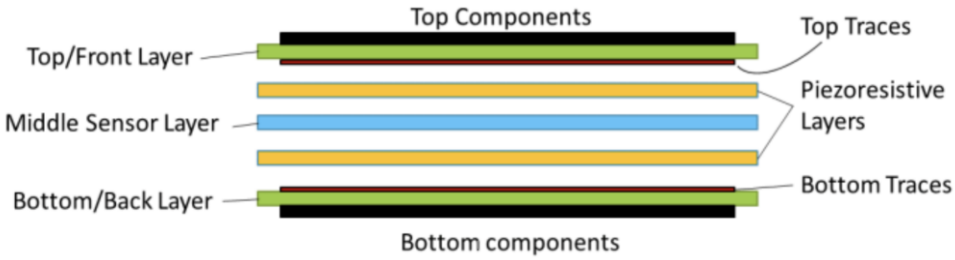

Figure 4.5: Drawing of the 5-layer design of Neuroskin and the overlap of the different layers.

The completed sensor array is shown below in Figure 4.6. Although the soldered components restricted the flexibility of the fPCB, the boards could still flex between sensor rows and columns due to the gap designed between oscillator circuits.

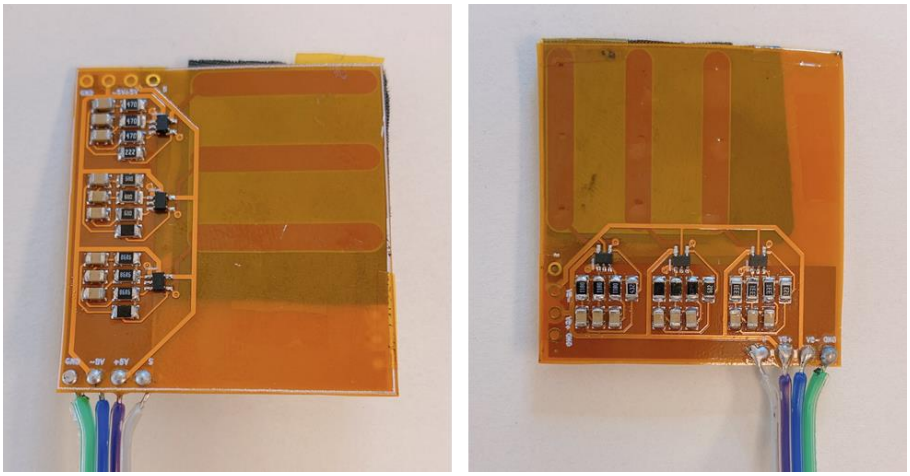

Figure 4.6: Images of the completed sensor array. Left image shows front of sensor array, and right image shows back of sensor array.

4.2 Sensor Characterization

To characterize the sensor the separability of the carrier waves was analyzed by Fourier transform and force-voltage response curves were obtained for each taxel.

The sensor was readout using a Teensy 4.1 [51] by taking 10-bit analog read measurements at a sampling frequency of 35 kHz. The carrier waves had high separability in a 1024-point FFT (Figure 4.7), and good separability in a 32-point FFT (Figure 4.8).

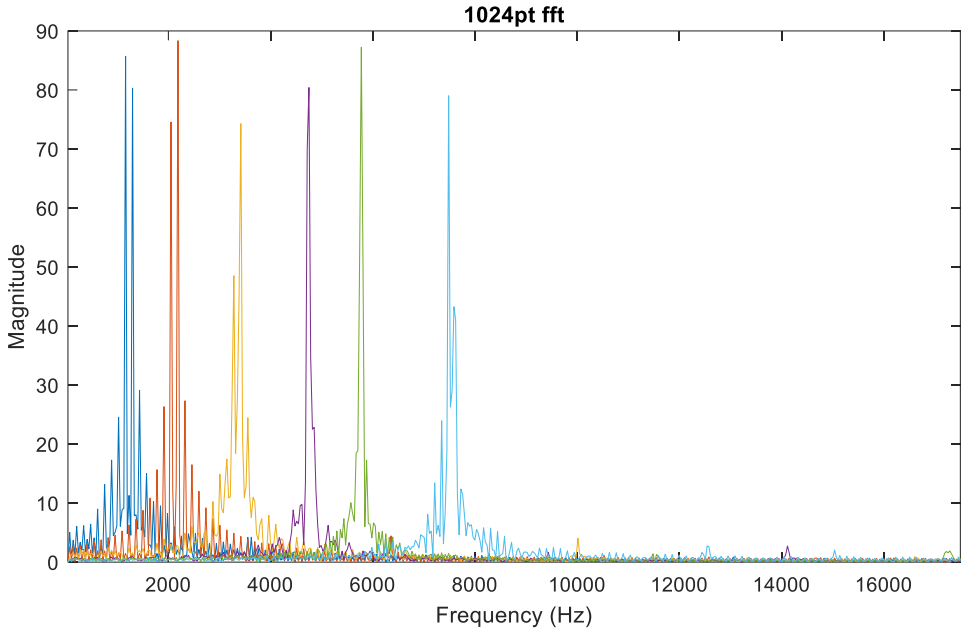

Figure 4.7: 1024-point FFT of the six carrier waves present in the sensor array. Plot shows a high separability in the different frequencies. The 1024-point FFT corresponds to ~30 msec of time.

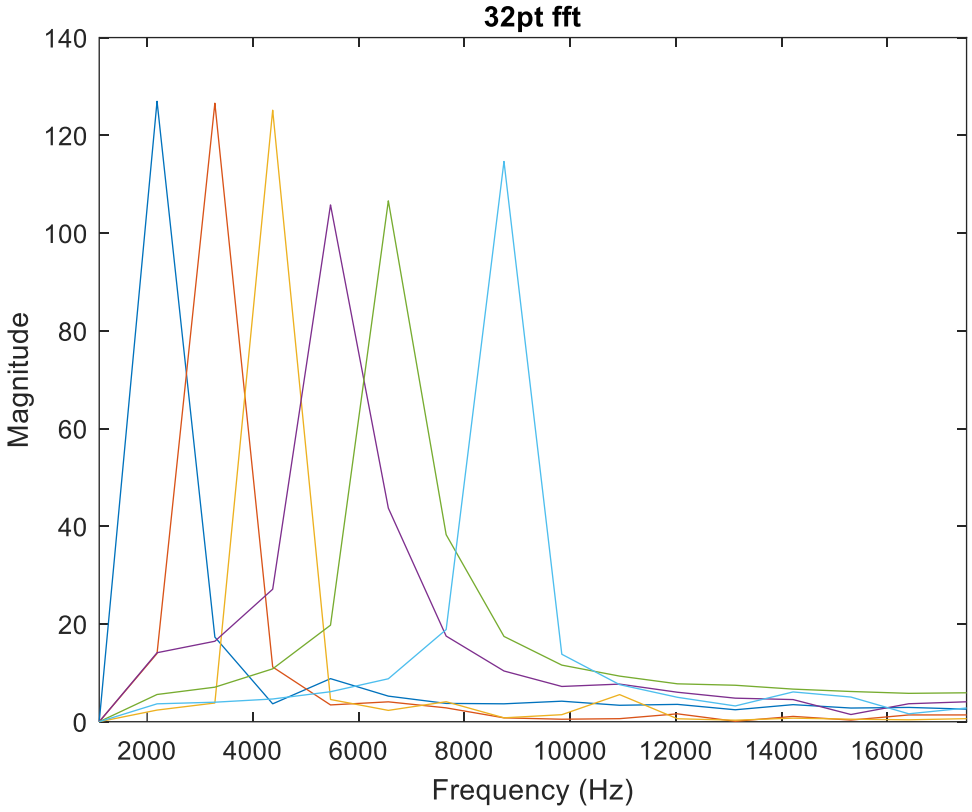

Figure 4.8: 32-point FFT of the six carrier waves present in the sensor array. Plot shows a high separability in the different frequencies. The 32-point FFT corresponds to 1 msec of time.

The 32-point FFT was used because the 32-point FFT corresponded to approximately 1 msec of time, which was the desired temporal resolution of the sensor, and still had a high degree of separability.

The force-voltage response was measured by applying different weights to each taxel of the sensor array and recording the outputted peak-to-peak voltage. A 3D printed tool was used to ensure consistent pressure on the sensor array, and weights ranging from 3.5 grams to 200 grams were used. The recorded responses are shown below in Figure 4.9. From the plot we can see that taxel 9 is less sensitive than the other taxels, but other

taxels generally behave similarly. Taxel 9 is likely less sensitive because it is physically closest to the perimeter circuitry, and therefore requires a larger weight to compress the piezoresistive fabric equivalently.

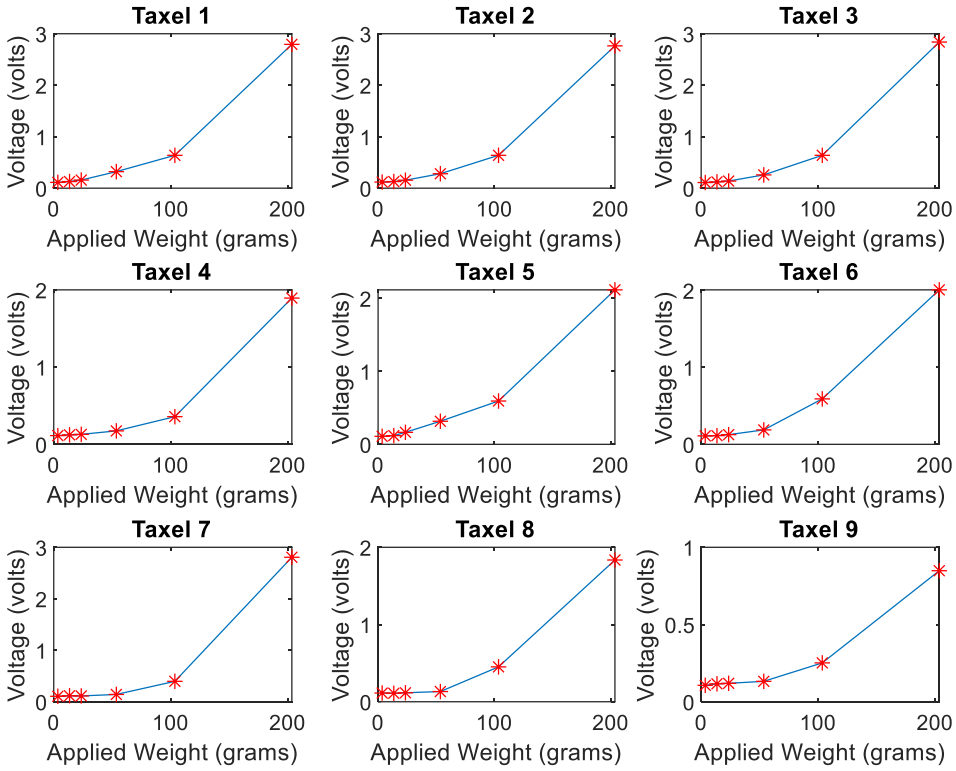

Figure 4.9: Taxel voltage response vs. applied weight. Plot shows response from 3.5g to 200g.

4.3 Texture Discrimination

Leveraging the high-speed and simultaneous sensing of Neuroskin 2, a texture discrimination task was performed.

To perform the texture discrimination task, the same methodology used in the Neuroskin 1 texture discrimination experiments was followed. This consisted of attaching the sensor array to a soft robotic biomimetic finger, attaching the sensorized finger to a

UR5 robotic arm, and palpating a library of 11 textures. Each texture was palpated 60 times leading to a total of 660 palpation trials. The same library of textures was used as the texture discrimination experiments of Neuroskin 1 (Figure 3.7). Frequency analysis was performed to reconstruct the pressure on the sensor array, and neuromorphic spike-based encoding was then used to reduce the dimensionality of the data and add robustness against trial-to-trial time misalignments.

After recording the voltage over time for all palpations of a specific texture, a cumulative sum metric was used to automatically divide each trial for classification (Figure 4.10). The cumulative sum curve was relatively smooth and had distinct peaks that lined up with the start of each palpation trial. A short time shift was also introduced into the cumulative sum curve, so each palpation was accurately captured without cutting off any of the data.

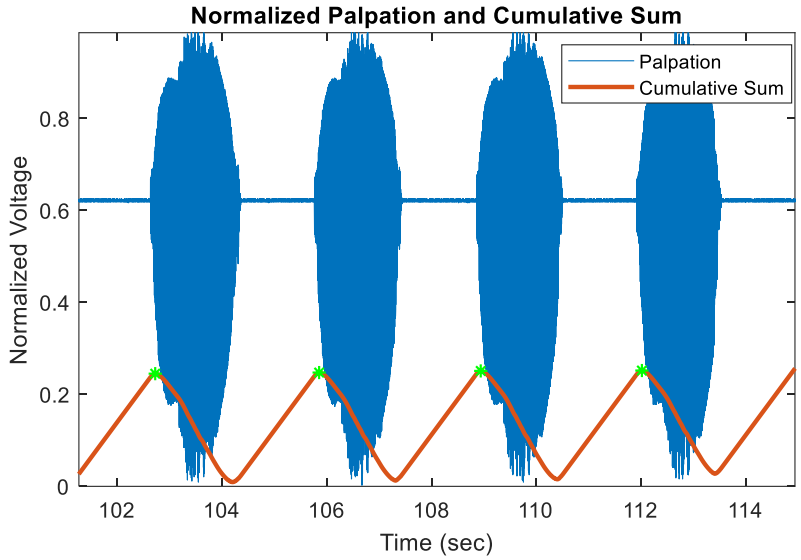

Figure 4.10: Normalized measured voltage (blue) and cumulative voltage sum (red) over time for three palpations. Peaks of the cumulative sum curve line up well with the start of each palpation. This alignment allows for automatic trial segmentation.

The cumulative sum metric separated the palpations well, and all trials can be visually inspected in the overlapped plot below (Figure 4.11). As seen in the plot, all textures created a unique voltage pattern that is visually distinguishable even prior to frequency analysis of the different carrier waves. This visual trend suggests that it may be possible to discriminate textures without doing frequency analysis, and by only analyzing the combined voltage waveform over time. This could be useful in online discrimination tasks where high-speed classification is necessary.

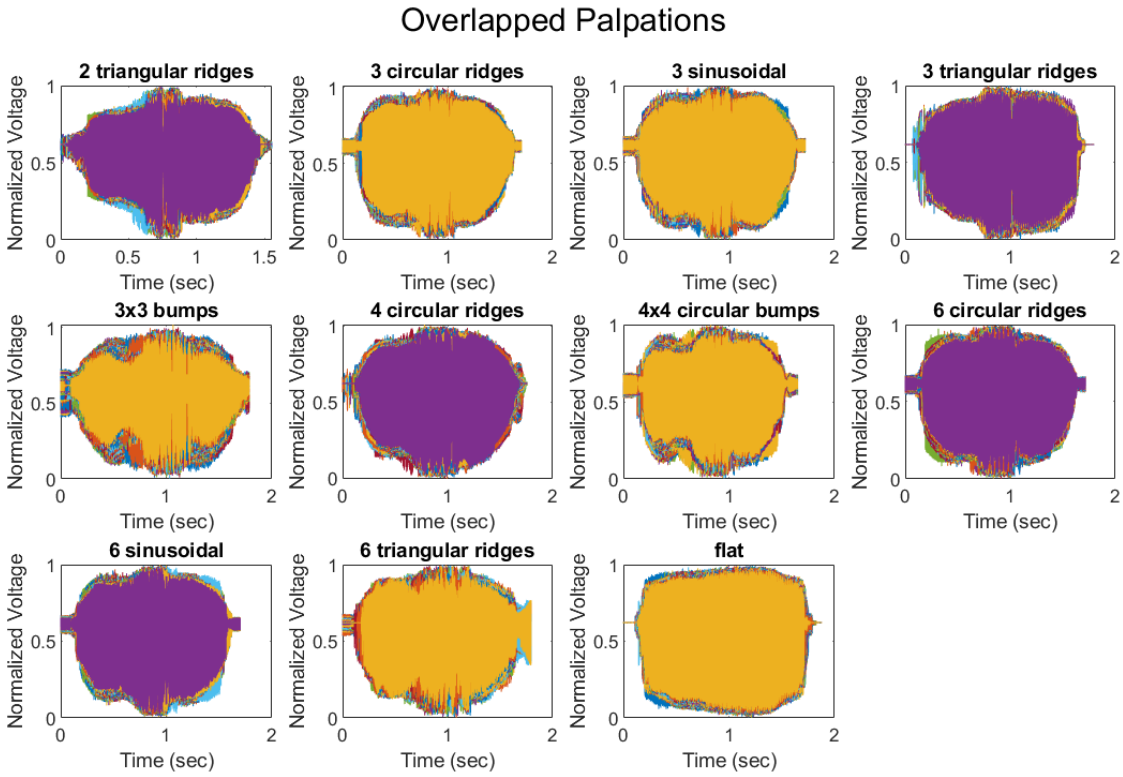

Figure 4.11: 60 overlapped palpations for each texture. General shapes of each texture can be inferred from the voltage profiles.

After segmenting all the trials, the frequency content of each palpation was analyzed to reconstruct the pressure profiles on the sensor array. The frequency analysis was done by computing a 32-point FFT and extracting the amplitudes of the six pertinent

frequencies over time (Figure 4.12). The 32-point FFT was computed with full overlap, and each consecutive time window differed by 1 sample. Thus, the total number of time windows was equal to the length of the palpation vector minus 32 (65,677 ≈ 1.88 seconds).

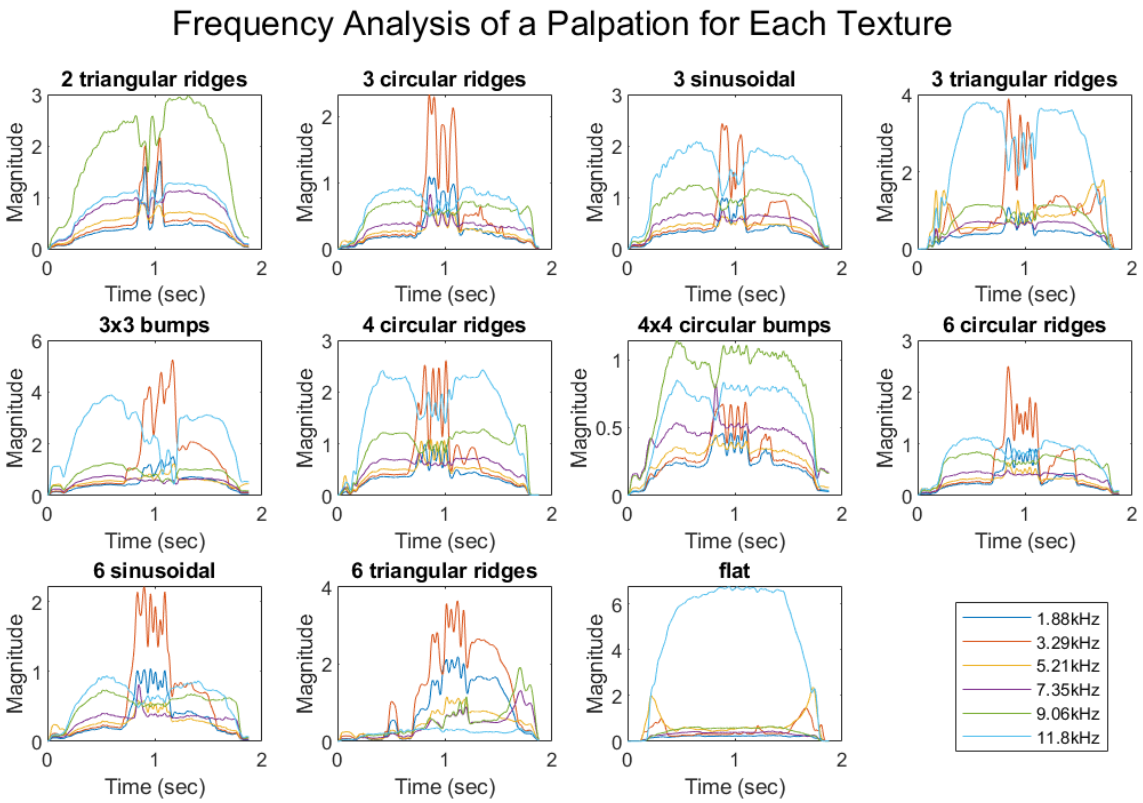

Figure 4.12: Frequency analysis of a palpation for each texture. The amplitudes of the six pertinent carrier frequencies are shown in each subplot over time.

After performing the frequency analysis, the dominant shape of the textures is visually clear. For example, a zoomed in section of a palpation of 3 circular ridges is highlighted below (Figure 4.13). As seen in the left plot, the profile of the 3 circular ridges texture can be seen in the 3 large bumps present in the dominant frequencies. The right figure shows the derivative of the left figure, further highlighting the texture profile.

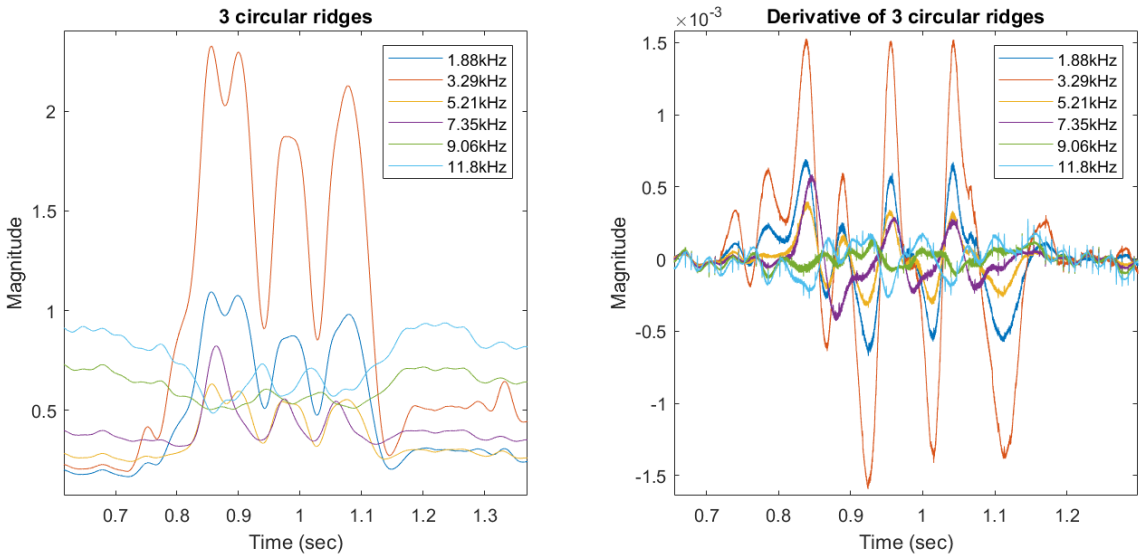

Figure 4.13: Zoomed in section of a palpation of the '3 circular ridges' texture. The pertinent frequencies are shown as different color curves, and the profile of the texture can be inferred from the relative amplitude changes over time. Left plot shows the amplitudes calculated from the FFTs, and the right plot shows the derivative of the plot.

The amplitudes of the six carrier frequencies are used to calculate the profile of each taxel on the sensor array, and the taxel values are then fed into an Izhikevich neuron model [48] to extract spike-based metrics for classification. The equations and effect of parameters is shown below in Figure 4.14. A rapidly adapting neuron model was utilized, and the corresponding parameters are shown below in Table 4.1. K is an added scaling factor for input current 'I', and tau is an added temporal scaling factor for v' and u'.

Table 4.1: Izhikevich parameters for a rapidly adapting neuron model.

Rapidly Adapting Neuron Model Parameters					
a	**b**	**c**	**d**	**tau**	**K**
0.02	0.25	-55	0.05	0.97	9

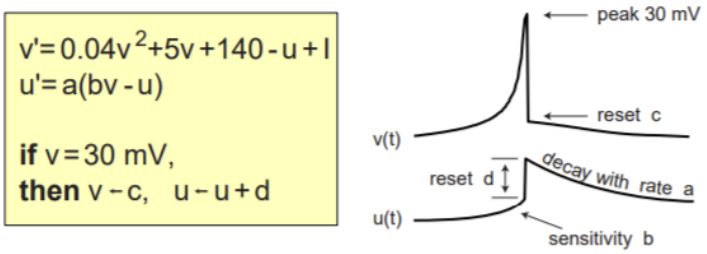

Figure 4.14: Differential equations for the Izhikevich model, and the effect of each parameter on the shape of the spike output. Reprinted from [48].

A kNN algorithm was used to classify the different textures (k=1). For each trial the mean inter-spike-interval (ISI), and ISI variance were obtained from the spike-encoded palpations and were then used as features for classification. Each palpation was plotted in this feature-space to visually show the separability of different textures. The plot is shown below in Figure 4.15 for taxel 1.

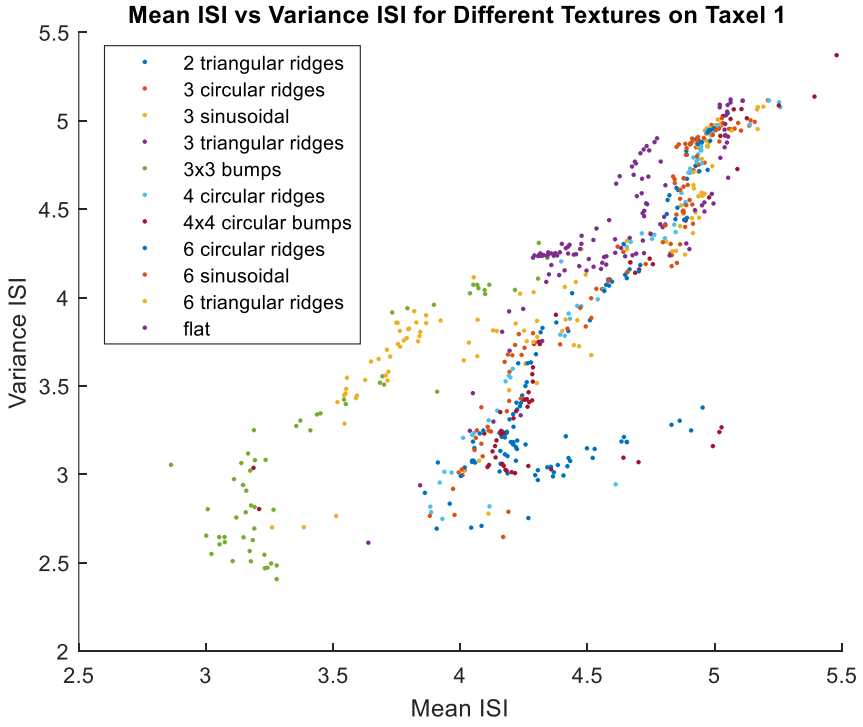

Figure 4.15: 2D feature-space plot of each palpation using the two spike-based metrics, mean ISI and ISI variance. Different colors represent the different labels of each palpation. The 3D renderings of the textures are found in Figure 3.7.

Because there are 9 taxels on the sensor and 2 spike-based features per taxel, each palpation was associated with 18 total features that were used in the classification algorithm. The KNN classification algorithm classified each palpation in this 18-dimensional space and calculated the assigned class labels based on Euclidean distance.

Overall, the sensor achieved high accuracy in discrimination, and had an average accuracy of 76.36%. K-fold cross validation was used to validate the result with a K value of 5, and the resulting confusion matrix is shown below in Figure 4.16.

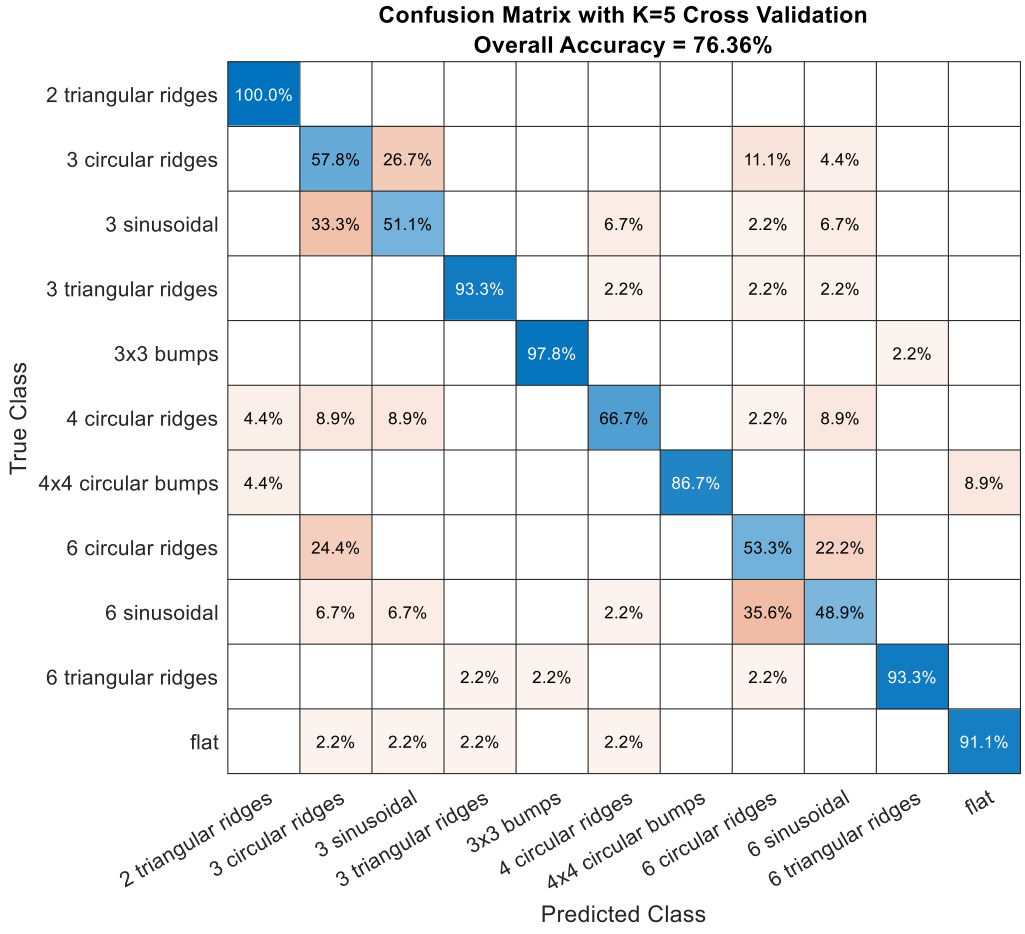

Figure 4.16: Confusion matrix for texture discrimination. Class numbers 1-11 correspond to textures: '2 triangular ridges', '3 circular ridges', '3 sinusoids', '3 triangular

ridges', '3x3 bumps', '4 circular ridges', '4x4 circular bumps', '6 circular ridges', '6 sinusoids', '6 triangular ridges', and 'flat' respectively.

4.4 Discussion and Conclusion

Neuroskin 2 provides a scalable platform for creating large area tactile sensor arrays with many sensing elements and a simple wiring scheme. Because Neuroskin 2 is developed in fPCB, it can readily be adopted by the community to scale up the design and enable sensorization of a variety of robotic devices.

Through compression of sensor data into row and column sums, the DTMF sensor not only simplifies wiring and allows for simultaneous sensor transmission but also allows for faster sensing than TDMA arrays of the same size. For example, a sensor array with $M * N$ taxels requires $M * N$ analog reads for a TDMA sensor (ignoring additional digital write time for row/column switching), but the equivalent DTMF readout only requires $(M + N) * 2$ analog reads (and no digital writes). This is a consequence of Nyquist sampling as we must sample the signal at least twice as fast as the fastest frequency. Thus, for all sensor arrays larger than 4x4, the DTMF readout is strictly faster than the TDMA readout. Furthermore, the reduction of wiring complexity makes the design of large arrays more feasible.

In this work, frequency analysis was done offline; however, an online-implementation could be realized using Goertzel algorithms that calculate the discrete Fourier transforms of specific frequencies as tactile data comes in [52]. Because of the DTMF-based design, the number of frequencies to analyze scales well with the number

of sensors making Neuroskin 2 quite promising for sensor arrays with numerous elements.

In the texture discrimination experiments, Neuroskin 2 performed slightly worse than Neuroskin 1. This can be attributed to the use of less flexible materials, a different machine learning algorithm, and the use of smaller decoding windows. Neuroskin 1 decoded the present frequencies in windows of ~100 msec, but Neuroskin 2 decoded in windows of 1 msec. While this made Neuroskin 2 have a higher temporal resolution, it also made it more susceptible to noise and other unexpected variations. Additionally, only two spike-features were used in classification (mean ISI and ISI variance) and increasing the number of features could also potentially increase the accuracy.

Because of the DTMF architecture, Neuroskin performs best when the inputs are sparse. Although the texture discrimination experiments conducted in this work did not have sparse inputs, real-world tactile stimuli are largely sparse [9], so Neuroskin could excel in deployment in prosthetic limbs or humanoid robots. Furthermore, because of the multi-layer design of Neuroskin, it could be possible to extract a multi-layer pressure response from the sensor array. This is possible due to the use of 2 piezoresistive layers in the design. This could enrich the tactile information captured by the sensor and could mimic the behavior of Type 1 and Type 2 mechanoreceptors in the human skin [2].

Additionally, Neuroskin 2 is a promising foundation for the development of sensor arrays for other sensing modalities past tactile. Thus, an interesting application would be to develop Neuroskin-like sensor arrays for the recording of neural activity from large areas populations of neurons or other sparse signals.

Overall Neuroskin is a scalable tactile sensor array that achieves millisecond temporal resolution, and simultaneous single-wire sensor transmission without the incorporation of electronics inside each taxel. Neuroskin is highly flexible and reproducible, allowing others to readily reproduce the device and scale it up to cover next-generation robotic devices with sophisticated tactile sensing skins.

Chapter 5

Continuing Work and Future Directions

This chapter summarizes the continuing work and future directions in which this work could potentially be taken forward.

5.1 Fabric-fPCB Hybrid Sensor

In addition to the fPCB-based sensor, Neuroskin 2, it is possible to develop a DTMF sensor array that is fully flexible, stretchable, made from fabric-based e-textile materials, and also uses fPCB to simplify wiring. Because the DTMF sensor array has no electronics inside each taxel, the copper traces in Neuroskin 2 can be replaced with conductive thread or fabric. This would enable the sensor to be designed to conform to almost any shape.

Therefore, a variant of the Neuroskin 2 fPCB was developed that lacked the middle sensing layer and the conductive row/column traces. This variant enables the same

scalable 4 wire design but allows the conductive traces to be replaced with e-textile fabric materials (Figure 5.1).

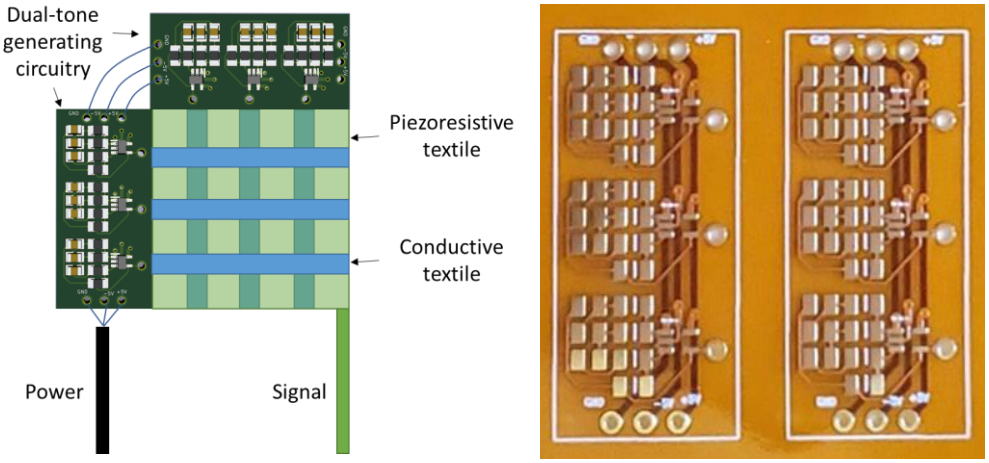

Figure 5.1: Fabric-fPCB hybrid sensor. Left shows drawing of an assembled sensor. Right shows produced fPCBs to be used in the perimeter of a fabric-fPCB hybrid sensor.

For example, a continuing work is creating a fabric-fPCB hybrid sensor that fully wraps around the soft robotic biomimetic finger. An example drawing of the prototype is shown below in Figure 5.2. Conductive thread or fabric is used to connect the power between one fPCB to another. By using this fPCB design, multiple fPCBs can be chained together to create arbitrarily shaped sensor arrays for a variety of applications.

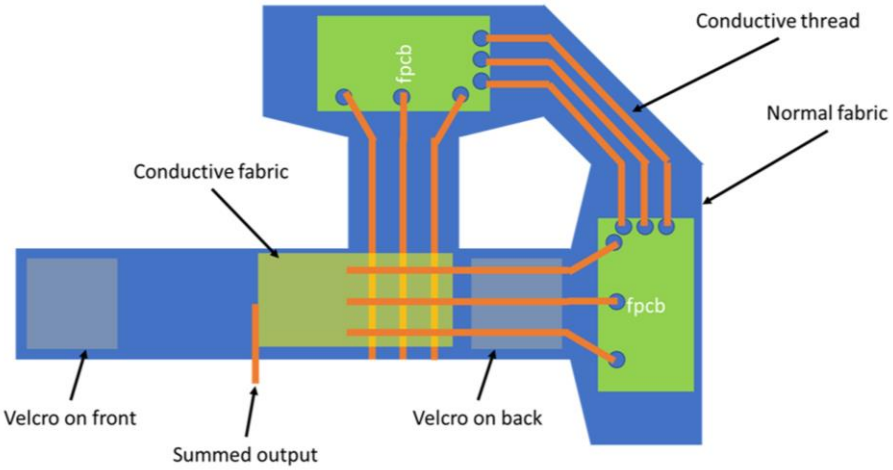

Figure 5.2: Drawing of fabric-fPCB hybrid sensor that can be completely wrapped around a prosthetic finger. Piezoresistive layer is not shown.

The drawing in Figure 5.2 was fabricated using spandex fabric and the e-textile materials used in Neuroskin 1. This fabric-fPCB hybrid design can be easily wrapped around a soft finger or other surface as shown below in Figure 5.3. Additionally, because all the power one fPCB to another is connected internally, the hybrid sensor still requires only one set of connection wires.

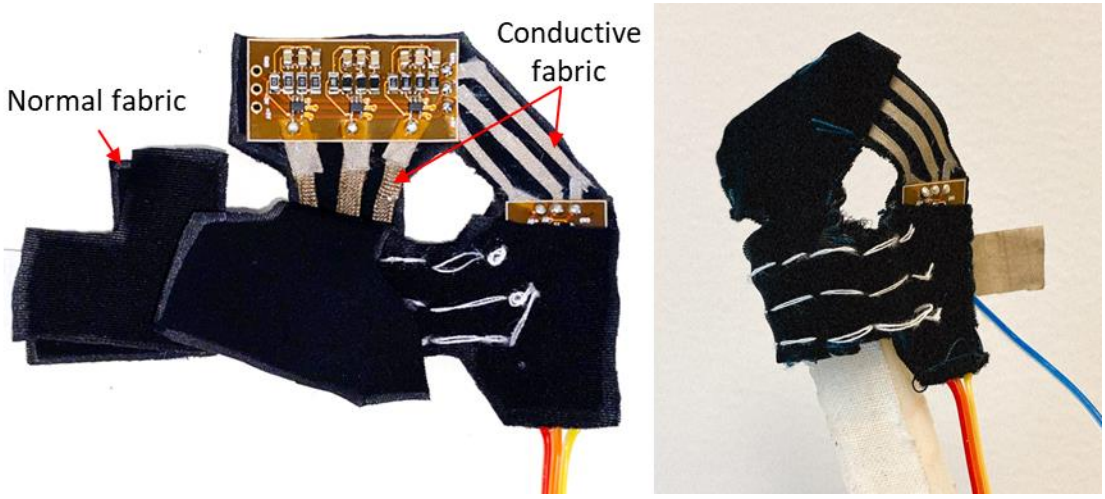

Figure 5.3: Image of hybrid sensor wrapped around a soft robotic biomimetic finger. Left image shows the sensor flat, and right image shows the sensor wrapped around the soft prosthetic finger.

5.2 Simultaneous multi-touch and error correction

A downside of using a DTMF-sensor array is that the sensor has ambiguity in multi-touch scenarios due to the under-deterministic nature of having more sensors than frequencies. To address this issue, a MATLAB simulation was conducted to investigate algorithms that could be used to correct multi-touch ambiguity as sensor readings were streamed. A 10x10 sensor was simulated in MATLAB and random pressures were applied to the different taxels in the sensor array with some random time delay between pressures. The pressures on each sensor were sustained over the course of the simulation to create multi-touch scenarios. Because different pressures started at different times, the simulation could decompose multi-touch scenarios into sequential single-touch scenarios. Without any algorithmic correction, readout of the sensor results in ambiguous readings and the detection of 'ghost' taxels that appear activated but did not have applied pressure. This ambiguity is seen below in Figure 5.4.

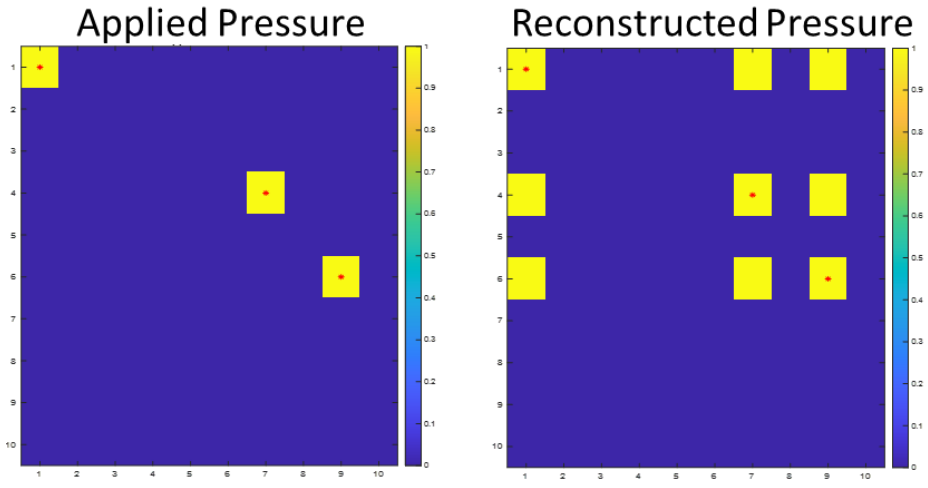

Figure 5.4: MATLAB simulation showing the application of 3 consecutive touches and the reconstructed pressures using a row/column reconstruction method. Left image shows applied pressure, and right image shows reconstructed image using row/column sums

(DTMF-based decoding). Notably the right image shows several ‘ghost’ taxels which appear activated but were not in reality. Red stars in the right image show the true locations of pressure.

As evident from the graph, although only 3 touches were made, the decoding algorithm identified 9 touches in total. This can be understood because the 3 touches resulted in 6 pertinent amplitude values. Then, using the current algorithm without error-correction, the pressure at each (row, column) intersection of the sensor array would be calculated by multiplying the amplitudes of the respective row and column. Thus, in the presented example where 3 row amplitudes and 3 column amplitudes are given, 9 taxel values are calculated.

To correct for this ambiguity, the decoding algorithm can leverage the high-speed of the DTMF sensor array and look at multi-touch problems as consecutive instances of single touches and store which sites are ‘active’. The current multi-touch solution uses the following pseudocode algorithm and a saved matrix of ‘active sites’ to address the multi-touch limitations:

```
1:   Calculate the difference in each row/column sum
2:   The current 'active site' is the (row, col) taxel
     with the highest difference
3:   Place the taxel into the active site matrix
4:   for each active site:
5:        calculate the pressure using the row/col sum
6:        if the pressure is below a threshold:
7:             remove active site and set to zero
8:        end
9:   end
```

This algorithm resolves multi-touch problems and allows for accurate reconstruction without ‘ghost’ taxels (Figure 5.5).

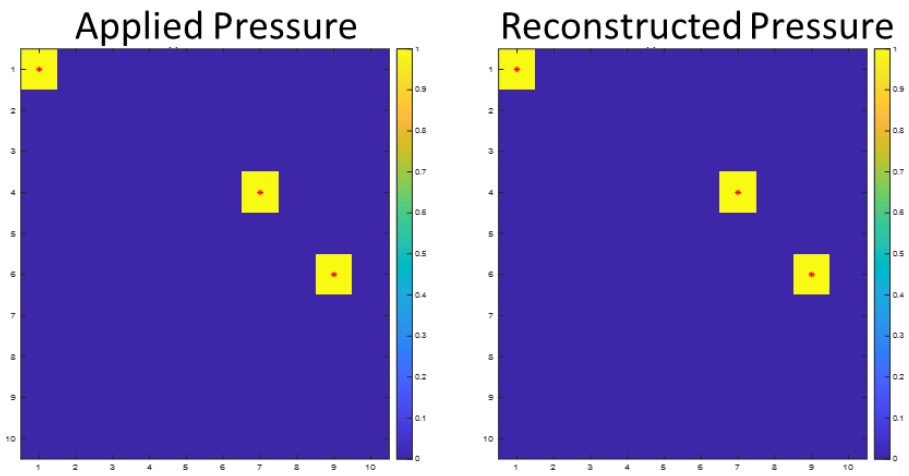

Figure 5.5: MATLAB simulation showing the application of 3 consecutive touches and the reconstructed pressures using a multi-touch error correction algorithm. Notably, the algorithm allows for correct reconstruction of the applied pressure.

However, this solution does not apply for true simultaneous multi-touch scenarios, and only works well if new touches are not registered at the same exact time.

Another current work is to correct the issue of true simultaneous multi-touch by reading each column independently. However, because this would increase wiring complexity and introduce latency, a single-wire strategy is desired. Therefore, ACES or other encoding algorithms can be used. For example, each row can be assigned a unique carrier frequency, and at the base of each column a microcontroller or digital signal processor can read the combined voltages from the column during touch interactions. Because each column is read individually, the number of frequencies is equivalent to the number of sensors, so there is no ambiguity for the identification of pressure locations. Then each column microcontroller can be designed to calculate the amplitudes of the different frequencies and output a spike code like the ACES receptors, or different sinusoids to sum onto a single wire. Then a decoder would read the combined signals and

reconstruct the applied pressures to the entire sensor array without any ambiguity. However, a trade-off in this solution is that it does not have innate data compression like the DTMF system and requires the number of spike codes to equal the number of sensors. Therefore, it is more computationally intensive than the DTMF-based encoding used in the current Neuroskin.

5.3 Sensorized prosthetic hand

Because Neuroskin 2 is theoretically more scalable than the conventional TDMA based sensor arrays, an ongoing work is to scale up Neuroskin to cover the surface of a prosthetic hand. Current work is focused on partnering with Infinite Biomedical Technologies to scale up the current fingertip sensors to cover the surface of a Taska prosthetic hand.

A preliminary fPCB design is shown below that allows for 170 sensing elements (Figure 5.6). However, this number can be greatly increased if smaller components are chosen. The 170-sensor design is using hand-solderable component sizes (0805).

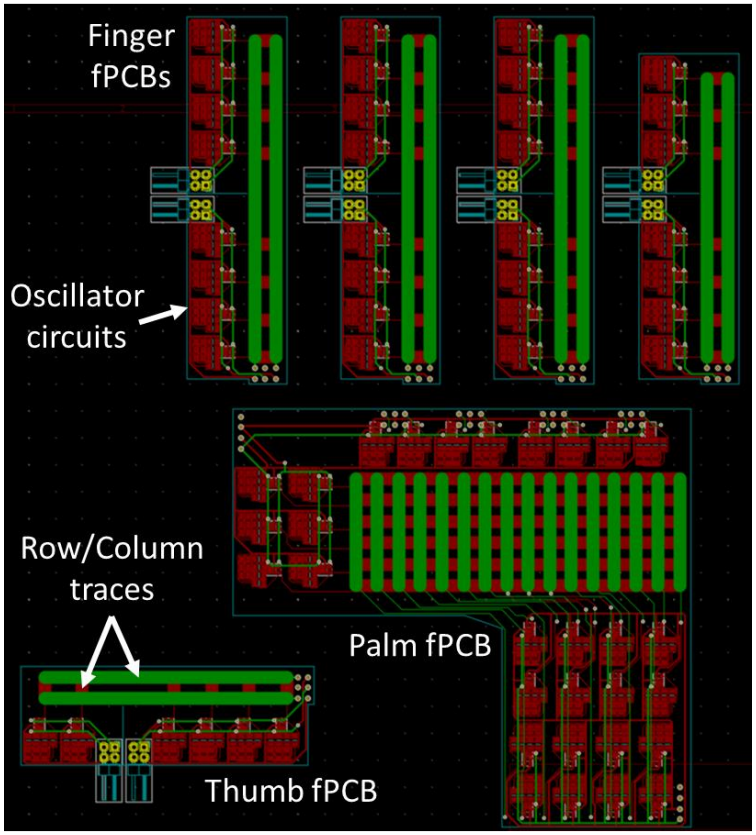

Figure 5.6: fPCB layout of a 170-sensor DTMF sensor array designed to cover the ventral side of the Taska prosthetic hand.

5.4 Real-time texture discrimination with SNN

The high-speed of Neuroskin can also be leveraged to perform a real-time texture discrimination task. Literature shows that spiking neural networks (SNN) are the most promising variety of neural networks for classifying dynamic temporal data [53] and most closely resemble the biological neural networks of our brain. Additionally, because SNNs classify data temporally, the network outputs spikes in the output layer immediately once input data is processed [53]. This makes SNNs classify objects quicker than CNNs and other artificial neural networks [54]. Furthermore, SNNs can be implemented in low power hardware to classify inputs in real-time. This makes SNNs

promising for real time texture discrimination. Preliminary work has focused on creating an offline SNN prior to converting it to an online network. A flow chart of the offline SNN discrimination is shown below (Figure 5.7).

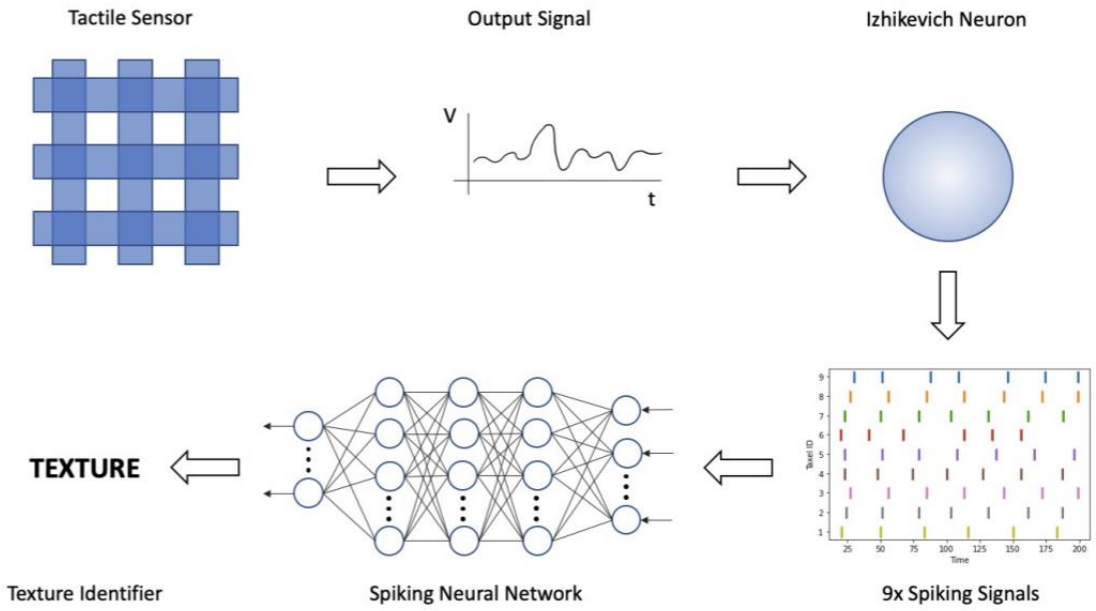

Figure 5.7: Flow chart of a spiking neural network texture classifier.

Our preliminary work on this goal has successfully developed an SNN to discriminate texture using a conventional TDMA based sensor. The Nengo SNN library [55] is implemented in python, and the network is constructed with 3 hidden layers of 256, 128, and 12 neurons. The activation functions for the first two layers are reLu and the final layer has a sigmoidal activation function. The current algorithm has achieved an accuracy of 99% on the preliminary dataset using a conventional TDMA tactile sensor (Figure 5.8). Current work focuses on converting the offline system to an online system

through hardware implementation on an FPGA where spectral analysis and texture discrimination will both be performed in real-time.

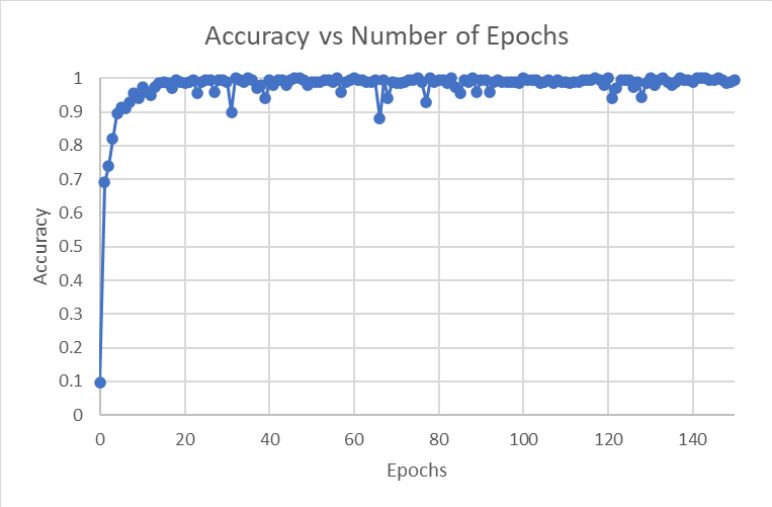

Figure 5.8: SNN accuracy for epoch number from the classification of a preliminary dataset using from a TDMA sensor.

5.5 Discussion and Conclusion

Spatial frequency encoded tactile sensor arrays have many promising future directions and ongoing works.

The use of e-textile materials demonstrates that the spatial frequency encoding architecture can support the use of flexible and unconventional materials. With further development this can be leveraged to create ultra-thin, conformal sensor arrays with other materials such as self-healing polymers. This directly improves on current asynchronous tactile sensor arrays that rely on the integration of electronics inside each taxel and therefore are not compatible with such materials.

The sensorization of the Taska prosthetic hand presents a useful application of the scalable sensing technology. Through the spatial frequency encoded sensor array, the sensorized prosthetic hand will have hundreds of sensors while retaining kilohertz temporal resolution, and simple wiring and readout. This technology can potentially be used to provide tactile feedback to amputees who lack tactile sensation in their prosthetic hand.

SNN is well suited to classify interactions with the spatial frequency encoded sensor due its high temporal resolution. Because SNNs perform well with dynamic time course data, they are useful for classifying real-world tactile interactions. Moreover, due to their fast classification, they can leverage the high speed of the tactile sensor to make accurate classifications in real-time. This would be particularly useful in the development of humanoid robots, as the spatial frequency encoded sensor can act as an artificial 'skin' and an SNN can act as an artificial 'brain' to make decisions based on tactile interactions.

Addressing the issue of multi-touch ambiguity is the most important step in proving the scalability of the spatial frequency encoded sensor. Therefore, the promising preliminary results of simultaneous multi-touch error-correction are significant for the development of larger sensors such as the sensor array designed for the sensorization of the Taska hand. Because the algorithm leverages the high speed of the sensor to decompose multi-touch scenarios into consecutive instances of single touch, the algorithm will perform better as the speed of the sensor is increased. Additionally, if event-based sensors are used that respond to changes in pressure rather than static

pressure (such as piezoelectric sensors), this would further simplify the error correction algorithm as fewer time instances will have many simultaneously responding sensors.

Overall, the results presented in this thesis demonstrate that the spatial frequency encoding sensing scheme is promising for the development of scalable tactile sensing systems. Through DTMF, the developed sensing scheme allows for simultaneous single-wire sensor transmission, the elimination of wiring complexity, the utilization of flexible materials, innate data compression, and does not require taxel-integrated electronics. Future tactile sensing systems may utilize the spatial frequency encoding architecture presented here to be dense, numerous, and flexible while retaining excellent temporal resolution.

Appendix

Review of sensing principles in tactile sensor arrays

TSAs have been developed using almost all modes of transduction [56]. This appendix section discusses the most common modes: piezoresistive, capacitive, optical, and piezoelectric.

Piezoresistive

Piezoresistive tactile sensors use piezoresistive materials that change their electrical resistance when pressures are applied [57]. These piezoresistive sensors are the most common type of sensor used in tactile sensing because of their wide scale availability, low cost, and high flexibility [58].

Over the years, a variety of piezoresistive tactile sensing arrays (TSA) have been developed; with many sensing arrays using row-column multiplexing to reduce wiring complexity [20]. By addressing each unit of the TSA by row/column indexing, the number of wires for a $m * n$ TSA is $m + n$ [59]. This is superior to non-multiplexed systems that require $m * n$ or $m * n + 1$ wires [60].

A potential downside of piezoresistive TSAs is that they suffer from non-linearity and have relatively high-power consumption because they are resistive sensors [61]. Piezoresistive sensors may also change their responses with temperature making them undesirable for certain applications [62]. Despite these downsides, piezoresistive sensors are robust against noise, and are good candidates for measuring static pressure [63]. Moreover, piezoresistive sensors have a very simple readout (voltage divider) [64]. These qualities make piezoresistive materials a good candidate for developing large sensing arrays.

Capacitive

Capacitive TSAs use capacitive materials that change their capacitance in response to pressure [65]. Typically, this is a consequence of mechanical forces that change the geometry of the capacitor [66]. For example, for a parallel plate capacitor, the capacitance is proportional to the plate area divided by the plate separation distance; and by adjusting either of these parameters the capacitance is affected [67].

Capacitive sensing arrays are widely used in robotics because they are sensitive and can be made very dense [67]. Capacitive TSAs are also not dependent on temperature like piezoresistive TSAs [65]. These qualities make them good candidates for developing high-density TSAs. However, making arrays with many elements is challenging due to parasitic capacitance from the wiring and other components [68].

An additional advantage of capacitive TSAs is their simple readout mechanism. To readout a capacitive TSA, the sensing elements are raster scanned and the capacitance

of each element is measured with a charge amplifier circuit [69]. Capacitive tactile sensors also have a wide dynamic range and have simple fabrication methods [70].

Optical

Optical sensors are among the most accurate tactile sensors due to their high resolution and have been shown to resolve surface roughness with 100nm resolution [71]. Optical sensors are generally constructed with deformable materials that conform to change the reflection/scattering of light onto a photodetector [72].

Optical sensors also enable the estimation of 3D force vectors and 3D displacement [73]. This is done using four quadrant photodiodes (and a pinhole) [73]. Measuring 3D force vectors is important in detecting incipient slip events as 3D forces can provide an estimate of the static friction coefficient [73].

These optical sensors generally have a more complicated readout mechanism because they rely on combinations of LEDs and photodetectors to transform the pressure signal to an electric signal. However, because the pressure signal is transduced optically the optical sensors are immune to electronic noise [73].

Piezoelectric

Piezoelectric sensors use piezoelectric materials that generate charge in response to applied pressure [74]. These sensors are great candidates for measuring dynamic pressures because they generate charge only during changes in pressure [75].

Recently piezoelectric nanowires have been developed with 100µm resolution [76]. These nanowires have enabled the production of extremely high-density tactile sensor arrays up to 8464 taxels per cm^2 [76].

Because piezoelectric sensors respond to dynamic pressure, they are good candidates for large sensing arrays with many elements. This is because of the inherent tactile data compression that dynamic sensors provide. This allows for tactile data over a large area to be represented by a sparse signal of on/off events.

Piezoelectric nanofibers have also been developed into yarns and other textile materials [77]. This allows for the integration of high-density tactile sensors into flexible textiles. This could be a good candidate for wearable tactile sensing skins made from fabric. Moreover, the readout mechanism for piezoelectric sensors is simple and consists of a charge amplifier like the capacitive sensors [78].

Summary

Table A.1: Summary of tactile sensing principles and their attributes and read out systems. Modified from Zou et al [63].

Sensing Principle	*Sensor attributes*	*Read out system*
Piezoresistive	High sensitivity and resolution Robust to noise In-situ structured sensor Susceptible to hysteresis	Highly integratable Highly Low complexity High portability High power consumption
Capacitive	High sensitivity and resolution Large dynamic measurement range Static and dynamic measurement Easily affected by noise	Highly integratable Medium complexity Medium power consumption High portability
Optical	High sensitivity Large dynamic range High frequency response High spatial resolution	Highly integrable Medium complexity Medium power consumption Medium portability
Piezoelectric	High sensitivity Large dynamic range High frequency response Dynamic measurements	Highly integratable Medium complexity High portability Medium power consumption

Implementation of Spatial Frequency Encoding

Spatial frequency encoding is implemented in four steps: carrier wave generation, wave modulation, signal integration, and decoding.

Carrier wave generation

To implement spatial frequency encoding, a large number of carrier waves must be generated at different frequencies. Electrically, carrier wave generation is accomplished through use of an electrical oscillator. These oscillator circuits can be built in a variety of ways.

The most popular sinusoidal oscillator circuits are the Wein bridge oscillator, the Colpitts crystal oscillator, and the phase shift oscillator [79]. These oscillators all use the concept of RC phase shift and an amplifier to generate a sinusoidal output. Three example circuits are shown below in Figure A.1.

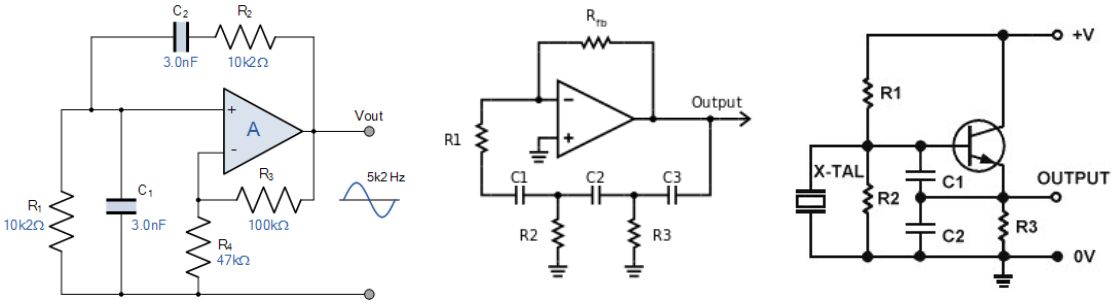

Figure A.1: Different sinusoidal oscillator circuits

In addition to electrical oscillator circuits, there are a variety of other methods to generate sinusoidal carrier waves electronically. One method is to use a square wave and filter the output [80]. Because square waves are composed of an infinite series of high

frequency sine waves, by low pass filtering the square wave we can recover a sinusoid. However, to achieve a sine wave with a high purity, a high order filter should be used. For example, a 5th order filtered square wave produces a sine wave with small error [81]. Another method is to use pulse combinations and low pass filtering [81]. For example, a PWM output can be low pass filtered to produce a sine wave [81].

The oscillators above are continuous, non-decaying oscillators. However, it is also possible to build oscillator circuits that produce decaying oscillations. While these circuits are not typically useful for telecommunications, they do hold promise for developing event-based tactile sensors. By incorporating exponential decay into the carrier wave, a static signal can be compressed into two events (onset and offset). This type of oscillator can be built using an LC tank circuit [81]. The LC tank circuit, or resonant/tuned circuit, produces an oscillating voltage due to the competing time constants of the parallel inductor and capacitor (Figure A.2). When the charged capacitor discharges across the inductor, a magnetic field is generated at the inductor. This magnetic field then dissipates into an induced voltage in the inductor. This recharges the capacitor, and the oscillations continue.

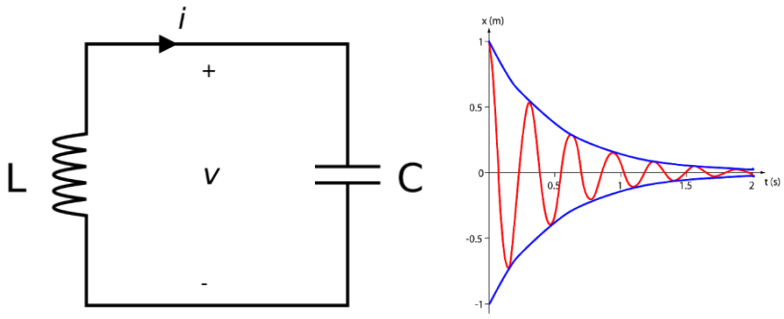

Figure A.2: Tank circuit and damped oscillations.

Non-electronic carrier waves can be generated as well. These carrier waves are either optical or acoustic. Light is inherently frequency encoded as different colors or wavelengths of light all have unique frequencies. Thus, a particular frequency of light can be used as a carrier wave for spatial frequency encoding. Likewise, acoustic waves are also inherently frequency encoded as different pitches have unique frequencies. Thus, a particular frequency of acoustic vibration can be used as a carrier wave for spatial frequency encoding.

Modulation

After a carrier wave is generated, it must be modulated to encode the sensor signal. This can be done through a variety of techniques; however, the most popular techniques are amplitude modulation (AM), frequency modulation (FM), and phase modulation (PM) [82] (Figure A.3).

Amplitude modulation is the simplest form of modulation and consists of simply changing the amplitude of the carrier wave to denote analog or digital data. This can be achieved through a variety of circuits including transistor circuits, voltage divider circuits, and more. Frequency modulation is another popular modulation variant. Rather than changing the signal amplitude to encode data, the carrier wave's frequency is adjusted to encode data. This method reduces the bandwidth of the network because the channel spacing between carrier waves must be increased to compensate for the frequency modulation spread. Frequency modulation is typically implemented in the carrier wave generator circuit, where the frequency of the signal is varied as the carrier wave is being generated. Phase modulation is another modulation variant used in WiFi

and wireless internet communication [83]. However, phase modulation and demodulation circuits are significantly more complicated and expensive than AM or FM circuits [84]. Moreover, PM is less robust than AM or FM, and is not used for long-range communication or in instances of emergency.

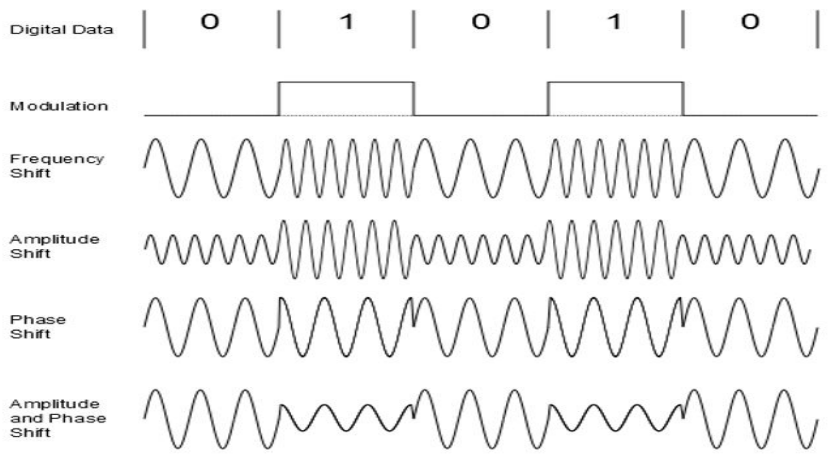

Figure A.3: Signal modulation methods. Reprinted from [82].

Integration

Because the sensors in spatial frequency encoding systems respond asynchronously, their signals must be combined into a single channel signal for analysis and decoding. To achieve this combination, a summing or mixing circuit is used [85].

Mixing circuits are typically built using operational amplifiers (op-amps) using the concept of virtual ground. By grounding the non-inverting input of the op-amp and completing the feedback loop between the op-amp output and the inverting input, the output of the op-amp follows the summation of the input signals present at the inverting terminal. The virtual ground is essential to ensure orthogonality between the different frequency signals. A derivation of this relationship can be seen below in Figure A.4.

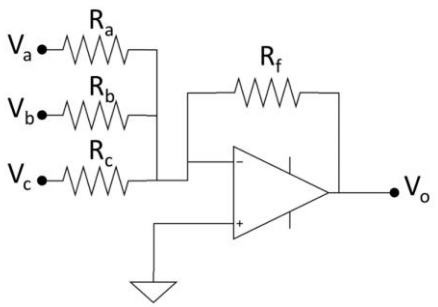

$$i_f = i_a + i_b + i_c$$

$$\frac{V_- - V_o}{R_f} = \frac{V_a - V_-}{R_a} + \frac{V_b - V_-}{R_b} + \frac{V_c - V_-}{Rc}$$

$$\frac{-V_o}{R_f} = \frac{V_a}{R_a} + \frac{V_b}{R_b} + \frac{V_c}{R_c}$$

$$\boldsymbol{V_o = -R_f\left(\frac{V_a}{R_a} + \frac{V_b}{R_b} + \frac{V_c}{R_c}\right)}$$

Figure A.4: Op-amp summation circuit and derivation.

To achieve accurate summing of signals, it is important for the op amp to respond at least twice as fast as the fastest frequency component being summed (Nyquist sampling). This speed parameter is referred to as the op-amps slew rate and represents the maximum rate of change of the op-amps output [86]. The gain bandwidth product (GBW) is also important if the op-amp is configured to have more than unity gain. Thus, in addition to having a high slew-rate the op amp must also have a GBW greater than the maximum frequency divided by the gain factor [87].

To integrate optical or acoustic the signals broadband receivers must be used. It is important to use a broadband receiver to ensure little biasing in the receiver, and ensure that all frequencies present are equally integrated by the receiver. For optical applications, these receivers are commonly used in spectroscopy to measure the presence of different frequencies in a sample of light [88]. For acoustic transduction, the integration is achieved by a broadband microphone [89]. These acoustic sensors capture the different frequencies present in the acoustic signal with equal weight for each frequency in the band of the microphone.

Decoding and analysis

To decode the integrated signal, mathematical techniques such as the Fourier transform can be employed [90]. This transform is used to decompose a function into its constituent frequencies. For spatial frequency encoding for tactile sensing systems, a real-time version of the Fourier transform should be used to realize the component frequencies in real time as they respond in the system. To achieve this, algorithms such as the real-time Fourier transform (RTFT) [91], or the fast Fourier transform (FFT) can be used [92]. A short time Fourier transform (STFT) that calculates the FFT in a sliding time window is shown below in Figure A.5.

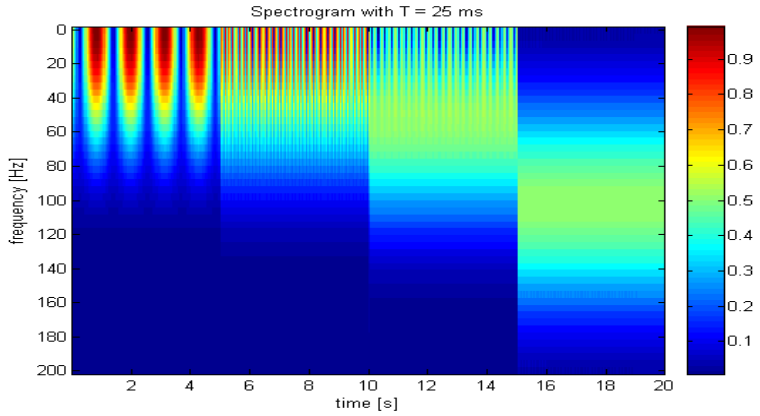

Figure A.5: Example of an STFT that calculates the frequency components over time using a sliding time window. Reprinted from [93].

To realize the FT in real time, these algorithms use windowing to calculate the discrete FT over a short time frame, with rates exceeding 1 kHz [94]. This time frame is limited by the computational speed of the algorithm and can be reduced by using fast graphical processing units (GPUs) or other fast computational tools such as FPGAs to achieve even faster processing rates [95].

The Fourier transform relies on the assumption that the input signal is a composition of a variety of sinusoidal signals with different frequencies and phases. If the signal is not composed of sinusoids, then other algorithms can be used for processing. For example, if spike rates are used to represent different sensor IDs biomimetically, then different mathematical methods can be more effective. Lee et al demonstrate this through their ACES architecture and use a neural network to accurately determine which sensors are responding [27].

Another method to realize the responding signals can be found in modern cellular communication. Modern cell phones use CDMA to allow for multiple users to communicate over the air simultaneously [95]. This method essentially uses the same assumption of combining orthogonal IDs, but rather the IDs are not sinusoids but specific bit sequences [95]. Then to decompose the signal into its constituent parts, a dot product is performed over a window of the signal with all the constituent IDs [95]. The ID with the highest dot product is assigned to that window. To resolve the issue of potential interference between simultaneously responding users, anti-collision protocols such as Aloha are used [96]. Aloha, or its improved version - slotted Aloha, incorporates a handshake between the sending user and the host to check to see if the message was received; and if the message failed due to collision it tries to send again until the packet has been received. A downside of this method is the user needs to be sophisticated enough to not only send packets but also receive packets (to determine whether a packet was sent). This is a potential complication for tactile sensing systems as it would require the integration of a signal processing unit into each taxel of the sensing system.

Otherwise, a central processing unit can distribute the different responses, but this would increase the wiring complexity.

Independent component analysis (ICA) is another attractive method for decoding [97]. ICA is similar to the FT but can use a variety of bases and is not limited to sinusoids. ICA functions under the assumption that the measured signal is composed of a linear sum of independent signals. A particularly useful variant of ICA is non-negative ICA (nnICA) [98]. nnICA has the added constraint that all the independent components are strictly added in the measured signal. This is particularly useful for real-world applications such as sound and voice separation, and particularly for spatial frequency encoding systems, because there is no subtractive process due to the orthogonality of the different responders. Real time ICA algorithms have been developed allowing for signal decoding with frequencies greater than 1kHz [99]. Like the FFT, these rates can be further improved through faster processing units or advanced GPUs [100].

References

[1] Kung, C. (2005). A possible unifying principle for mechanosensation. Nature, 436(7051), 647–654. https://doi.org/10.1038/nature03896

[2] Burgess, P. R., & Perl, E. R. (1973). Cutaneous Mechanoreceptors and Nociceptors. In Somatosensory System (pp. 29–78). Springer Berlin Heidelberg. https://doi.org/10.1007/978-3-642-65438-1_3

[3] Naitoh, Y., & Eckert, R. (1969). Ionic Mechanisms Controlling Behavioral Responses of Paramecium to Mechanical Stimulation. Science, 164(3882), 963–965. https://doi.org/10.1126/science.164.3882.963

[4] Whiting, J., Mayne, R., & Adamatzky, A. (2018). A Parallel Modular Biomimetic Cilia Sorting Platform. Biomimetics, 3(2), 5. https://doi.org/10.3390/biomimetics3020005

[5] Ludeman, D. A., Farrar, N., Riesgo, A., Paps, J., & Leys, S. P. (2014). Evolutionary origins of sensation in metazoans: functional evidence for a new sensory organ in sponges. BMC Evolutionary Biology, 14(1), 3. https://doi.org/10.1186/1471-2148-14-3

[6] Monshausen, G. B., & Gilroy, S. (2009). Feeling green: mechanosensing in plants. Trends in Cell Biology, 19(5), 228–235. https://doi.org/10.1016/j.tcb.2009.02.005

[7] Catton, W. T. (1970). Mechanoreceptor function. Physiological Reviews, 50(3), 297–318. https://doi.org/10.1152/physrev.1970.50.3.297

[8] Lehtinen, S. (2018). Understanding the Venus flytrap through mathematical modelling. Journal of Theoretical Biology, 444, 1–10. https://doi.org/10.1016/j.jtbi.2018.02.003

[9] Lee, W. W., Kukreja, S. L., & Thakor, N. V. (2017). Discrimination of Dynamic Tactile Contact by Temporally Precise Event Sensing in Spiking Neuromorphic Networks. Frontiers in Neuroscience, 11. https://doi.org/10.3389/fnins.2017.00005

[10] Lamb, G. D. (1983). Tactile discrimination of textured surfaces: peripheral neural coding in the monkey. The Journal of Physiology, 338(1), 567–587. https://doi.org/10.1113/jphysiol.1983.sp014690

[11] Miyaoka, T., Mano, T., & Ohka, M. (1999). Mechanisms of fine-surface-texture discrimination in human tactile sensation. The Journal of the Acoustical Society of America, 105(4), 2485–2492. https://doi.org/10.1121/1.426852

[12] Johansson, R. S., & Vallbo, A. B. (1979). Tactile sensibility in the human hand: relative and absolute densities of four types of mechanoreceptive units in glabrous skin. The Journal of Physiology, 286(1), 283–300. https://doi.org/10.1113/jphysiol.1979.sp012619

[13] Skedung, L., Arvidsson, M., Chung, J. Y., Stafford, C. M., Berglund, B., & Rutland, M. W. (2013). Feeling Small: Exploring the Tactile Perception Limits. Scientific Reports, 3(1). https://doi.org/10.1038/srep02617

[14] Carpenter, C. W., Dhong, C., Root, N. B., Rodriquez, D., Abdo, E. E., Skelil, K., Alkhadra, M. A., Ramírez, J., Ramachandran, V. S., & Lipomi, D. J. (2018). Human ability to discriminate surface chemistry by touch. Materials Horizons, 5(1), 70–77. https://doi.org/10.1039/c7mh00800g

[15] Howe, R. D. (1993). Tactile sensing and control of robotic manipulation. Advanced Robotics, 8(3), 245–261. https://doi.org/10.1163/156855394x00356

[16] Valle, G., Mazzoni, A., Iberite, F., D'Anna, E., Strauss, I., Granata, G., Controzzi, M., Clemente, F., Rognini, G., Cipriani, C., Stieglitz, T., Petrini, F. M., Rossini, P. M., & Micera, S. (2018). Biomimetic Intraneural Sensory Feedback Enhances Sensation Naturalness, Tactile Sensitivity, and Manual Dexterity in a Bidirectional Prosthesis. Neuron, 100(1), 37-45.e7. https://doi.org/10.1016/j.neuron.2018.08.033

[17] Snyder, W. E., & St. Clair, J. (1978). Conductive Elastomers as Sensor for Industrial Parts Handling Equipment. IEEE Transactions on Instrumentation and Measurement, 27(1), 94–99. https://doi.org/10.1109/tim.1978.4314628

[18] Day, N., Penaloza, J., Santos, V. J., & Killpack, M. D. (2018). Scalable fabric tactile sensor arrays for soft bodies. Journal of Micromechanics and Microengineering, 28(6), 064004. https://doi.org/10.1088/1361-6439/aab221

[19] Lee, W. W., Cabibihan, J., & Thakor, N. V. (2013, November). Bio-mimetic strategies for tactile sensing. 2013 IEEE SENSORS. 2013 IEEE Sensors. https://doi.org/10.1109/icsens.2013.6688260

[20] Lee, W. W., Kukreja, S. L., & Thakor, N. V. (2015, October). A kilohertz kilotaxel tactile sensor array for investigating spatiotemporal features in neuromorphic touch. 2015 IEEE Biomedical Circuits and Systems Conference (BioCAS). 2015 IEEE Biomedical Circuits and Systems Conference (BioCAS). https://doi.org/10.1109/biocas.2015.7348412

[21] Johansson, R. S., & Birznieks, I. (2004). First spikes in ensembles of human tactile afferents code complex spatial fingertip events. Nature Neuroscience, 7(2), 170–177. https://doi.org/10.1038/nn1177

[22] Taunyazov, T., Sng, W., See, H. H., Lim, B., Kuan, J., Ansari, A. F., Tee, B. C. K., & Soh, H. (2020, September 15). Event-Driven Visual-Tactile Sensing and Learning for Robots. arXiv.org. https://arxiv.org/abs/2009.07083.

[23] Sundaram, S., Kellnhofer, P., Li, Y., Zhu, J.-Y., Torralba, A., & Matusik, W. (2019). Learning the signatures of the human grasp using a scalable tactile glove. Nature, 569(7758), 698–702. https://doi.org/10.1038/s41586-019-1234-z

[24] Inaba, M., Hoshino, Y., Nagasaka, K., Ninomiya, T., Kagami, S., & Inoue, H. (n.d.). A full-body tactile sensor suit using electrically conductive fabric and strings. Proceedings of IEEE/RSJ International Conference on Intelligent Robots and Systems.

IROS ’96. IEEE/RSJ International Conference on Intelligent Robots and Systems. IROS ’96. https://doi.org/10.1109/iros.1996.570816

[25] Mittendorfer, P., Yoshida, E., & Cheng, G. (2015). Realizing whole-body tactile interactions with a self-organizing, multi-modal artificial skin on a humanoid robot. Advanced Robotics, 29(1), 51-67.

[26] Oballe-Peinado, O., Hidalgo-Lopez, J. A., Castellanos-Ramos, J., Sanchez-Duran, J. A., Navas-Gonzalez, R., Herran, J., & Vidal-Verdu, F. (2017). FPGA-Based Tactile Sensor Suite Electronics for Real-Time Embedded Processing. IEEE Transactions on Industrial Electronics, 64(12), 9657–9665. https://doi.org/10.1109/tie.2017.2714137

[27] Lee, W. W., Tan, Y. J., Yao, H., Li, S., See, H. H., Hon, M., ... & Tee, B. C. (2019). A neuro-inspired artificial peripheral nervous system for scalable electronic skins. Science Robotics, 4(32).

[28] Cassidy, A., & Ekanayake, V. (2006, November). A biologically inspired tactile sensor array utilizing phase-based computation. In 2006 IEEE Biomedical Circuits and Systems Conference (pp. 45-48). IEEE.

[29] Johansson, R. S., & Flanagan, J. R. (2009). Coding and use of tactile signals from the fingertips in object manipulation tasks. Nature Reviews Neuroscience, 10(5), 345-359.

[30] Slepyan, A., & Thakor, N. (2020, November). Towards scalable soft e-skin: Flexible event-based tactile-sensors using wireless sensor elements embedded in soft

elastomer. In 2020 8th IEEE RAS/EMBS International Conference for Biomedical Robotics and Biomechatronics (BioRob) (pp. 334-339). IEEE.

[31] NXP Semiconductors (2017). Kinetis KL03 32 KB Flash. https://www.nxp.com/docs/en/data-sheet/KL03P24M48SF0.pdf

[32] Usami, M., Tanabe, H., Sato, A., Sakama, I., Maki, Y., Iwamatsu, T., Ipposhi, T., & Inoue, Y. (2007, February). A 0.05×0.05mm2 RFID Chip with Easily Scaled-Down ID-Memory. 2007 IEEE International Solid-State Circuits Conference. Digest of Technical Papers. 2007 IEEE International Solid-State Circuits Conference. https://doi.org/10.1109/isscc.2007.373504

[33] Dumez, J.-N. (2018). Spatial encoding and spatial selection methods in high-resolution NMR spectroscopy. Progress in Nuclear Magnetic Resonance Spectroscopy, 109, 101–134. https://doi.org/10.1016/j.pnmrs.2018.08.001

[34] Orthogonality of Sinusoids: Mathematics of the DFT. DSP. (n.d.). https://www.dsprelated.com/freebooks/mdft/Orthogonality_Sinusoids.html.

[35] Weinstein, S., & Ebert, P. (1971). Data Transmission by Frequency-Division Multiplexing Using the Discrete Fourier Transform. IEEE Transactions on Communication Technology, 19(5), 628–634. https://doi.org/10.1109/tcom.1971.1090705

[36] Lustig, M., Donoho, D. L., Santos, J. M., & Pauly, J. M. (2008). Compressed Sensing MRI. IEEE Signal Processing Magazine, 25(2), 72–82. https://doi.org/10.1109/msp.2007.914728

[37] Mansfield, P., & Maudsley, A. A. (1977). Medical imaging by NMR. The British journal of radiology, 50(591), 188-194. MRI figure - http://mriquestions.com/frequency-encoding.html

[38] Valenti, M. C., & Chandran, N. (2001). Three generations of cellular wireless systems. https://eeweb.engineering.nyu.edu/~yao/EE3414_S03/Cellular.pdf

[39] Introduction to Digital Communications. (2016). Elsevier. https://doi.org/10.1016/c2012-0-06171-6

[40] Chen, W.-K. (2002). The electrical engineering handbook. Academic Press.

[41] Sklar, B., & Harris, F. J. (1988). Digital communications: fundamentals and applications (Vol. 2). Englewood Cliffs, NJ: Prentice-hall.

[42] Schenker, L. (1960). Pushbutton Calling with a Two-Group Voice-Frequency Code. Bell System Technical Journal, 39(1), 235–255. https://doi.org/10.1002/j.1538-7305.1960.tb03929.x

[43] Rajan, C., Megala, B., Nandhini, A., & Priya, C. R. (2015). A Review: Comparative Analysis of Arduino Micro Controllers in Robotic Car. vol, 9, 371-380.

[44] Slepyan, A., Sankar, S., & Thakor, N. (2021, May 4). Texture Discrimination Using a Neuromimetic Asynchronous Flexible Tactile Sensor Array with Spatial Frequency Encoding. 2021 10th International IEEE/EMBS Conference on Neural Engineering (NER). 2021 10th International IEEE/EMBS Conference on Neural Engineering (NER). https://doi.org/10.1109/ner49283.2021.9441136

[45] Osborn, L., Lee, W. W., Kaliki, R., & Thakor, N. (2014, August). Tactile feedback in upper limb prosthetic devices using flexible textile force sensors. In 5th IEEE RAS/EMBS International Conference on Biomedical Robotics and Biomechatronics (pp. 114-119). IEEE.

[46] Osborn, L. E., Dragomir, A., Betthauser, J. L., Hunt, C. L., Nguyen, H. H., Kaliki, R. R., & Thakor, N. V. (2018). Prosthesis with neuromorphic multilayered e-dermis perceives touch and pain. Science robotics, 3(19).

[47] Sankar, S., Brown, A., Balamurugan, D., Nguyen, H., Iskarous, M., Simcox, T., ... & Thakor, N. (2019, October). Texture Discrimination using a Flexible Tactile Sensor Array on a Soft Biomimetic Finger. In 18th IEEE Sensors, SENSORS 2019 (p. 8956704). Institute of Electrical and Electronics Engineers Inc.

[48] Izhikevich, E. M. (2003). Simple model of spiking neurons. IEEE Transactions on neural networks, 14(6), 1569-1572

[49] KiCAD 5.1.10. https://www.kicad.org/

[50] PCBWay. China. https://www.pcbway.com/

[51] Teensy 4.1 PJRC. https://www.pjrc.com/store/teensy41.html

[52] Chicharo, J. F., & Kilani, M. T. (1996). A sliding Goertzel algorithm. Signal Processing, 52(3), 283-297.

[53] Ghosh-Dastidar, S., & Adeli, H. (2009). Third Generation Neural Networks: Spiking Neural Networks. In Advances in Intelligent and Soft Computing (pp. 167–178). Springer Berlin Heidelberg. https://doi.org/10.1007/978-3-642-03156-4_17

[54] Taunyazov, T., Chua, Y., Gao, R., Soh, H., & Wu, Y. (2020, October 24). Fast Texture Classification Using Tactile Neural Coding and Spiking Neural Network. 2020 IEEE/RSJ International Conference on Intelligent Robots and Systems (IROS). 2020 IEEE/RSJ International Conference on Intelligent Robots and Systems (IROS). https://doi.org/10.1109/iros45743.2020.9340693

[55] Bekolay, T., Bergstra, J., Hunsberger, E., DeWolf, T., Stewart, T. C., Rasmussen, D., Choo, X., Voelker, A. R., & Eliasmith, C. (2014). Nengo: a Python tool for building large-scale functional brain models. Frontiers in Neuroinformatics, 7. https://doi.org/10.3389/fninf.2013.00048

[56] Dahiya, R. S., & Valle, M. (2012). Robotic tactile sensing: technologies and system. Springer Science & Business Media.

[57] Fiorillo, A. S. (1997). A piezoresistive tactile sensor. IEEE Transactions on Instrumentation and Measurement, 46(1), 15–17. https://doi.org/10.1109/19.552150

[58] Stassi, S., Cauda, V., Canavese, G., & Pirri, C. (2014). Flexible Tactile Sensing Based on Piezoresistive Composites: A Review. Sensors, 14(3), 5296–5332. https://doi.org/10.3390/s140305296

[59] Nicholls, H. R., & Lee, M. H. (1989). A Survey of Robot Tactile Sensing Technology. The International Journal of Robotics Research, 8(3), 3–30. https://doi.org/10.1177/027836498900800301

[60] Raibert, M. H., & Tanner, J. E. (1982). Design and Implementation of a VLSI Tactile Sensing Computer. The International Journal of Robotics Research, 1(3), 3–18. https://doi.org/10.1177/027836498200100301

[61] Kanda, Y. (1991). Piezoresistance effect of silicon. Sensors and Actuators A: Physical, 28(2), 83–91. https://doi.org/10.1016/0924-4247(91)85017-i

[62] Sea-Chung Kim, & Wise, K. D. (1983). Temperature sensitivity in silicon piezoresistive pressure transducers. IEEE Transactions on Electron Devices, 30(7), 802–810. https://doi.org/10.1109/t-ed.1983.21213

[63] Zou, L., Ge, C., Wang, Z., Cretu, E., & Li, X. (2017). Novel Tactile Sensor Technology and Smart Tactile Sensing Systems: A Review. Sensors, 17(11), 2653. https://doi.org/10.3390/s17112653

[64] Tise, B. (1988). A compact high resolution piezoresistive digital tactile sensor. Proceedings. 1988 IEEE International Conference on Robotics and Automation. Proceedings. 1988 IEEE International Conference on Robotics and Automation. https://doi.org/10.1109/robot.1988.12150

[65] Zhu, F., & Spronck, J. W. (1992). A capacitive tactile sensor for shear and normal force measurements. Sensors and Actuators A: Physical, 31(1–3), 115–120. https://doi.org/10.1016/0924-4247(92)80089-l

[66] https://patents.google.com/patent/US5225959A/en

[67] Gray, B. L., & Fearing, R. S. (1996, April). A surface micromachined microtactile sensor array. In Proceedings of IEEE International Conference on Robotics and Automation (Vol. 1, pp. 1-6). IEEE.

[68] Heerens, W. C. (1986). Application of capacitance techniques in sensor design. Journal of physics E: Scientific instruments, 19(11), 897.

[69] Peng, S. Y., & Hasler, P. E. (2008). U.S. Patent No. 7,339,384. Washington, DC: U.S. Patent and Trademark Office.

[70] Hotelling, S. P., & Elias, J. P. (2015). U.S. Patent No. 9,201,547. Washington, DC: U.S. Patent and Trademark Office.

[71] Ahmadi, R., Arbatani, S., Ozhikandathil, J., Packirisamy, M., & Dargahi, J. (2015). A multi-purpose optical microsystem for static and dynamic tactile sensing. Sensors and Actuators A: Physical, 235, 37–47. https://doi.org/10.1016/j.sna.2015.09.035

[72] Nomura, A., Abiko, I., Shibata, I., Watanabe, T., & Nihei, K. (1985). Two-Dimensional Tactile Sensor Using Optical Method. IEEE Transactions on Components, Hybrids, and Manufacturing Technology, 8(2), 264–268. https://doi.org/10.1109/tchmt.1985.1136496

[73] Khamis, H., Xia, B., & Redmond, S. J. (2019). A novel optical 3D force and displacement sensor – Towards instrumenting the PapillArray tactile sensor. Sensors and Actuators A: Physical, 291, 174–187. https://doi.org/10.1016/j.sna.2019.03.051

[74] Dahiya, R. (2015). Piezoelectric Tactile Sensors. In Wiley Encyclopedia of Electrical and Electronics Engineering (pp. 1–15). John Wiley & Sons, Inc. https://doi.org/10.1002/047134608x.w8243

[75] Yu, P., Liu, W., Gu, C., Cheng, X., & Fu, X. (2016). Flexible Piezoelectric Tactile Sensor Array for Dynamic Three-Axis Force Measurement. Sensors, 16(6), 819. https://doi.org/10.3390/s16060819

[76] Wu, W., Wen, X., & Wang, Z. L. (2013). Taxel-Addressable Matrix of Vertical-Nanowire Piezotronic Transistors for Active and Adaptive Tactile Imaging. Science, 340(6135), 952–957. https://doi.org/10.1126/science.1234855

[77] Hsu, Y.-H., Liu, P.-C., Lin, T.-T., Huang, S.-W., & Lai, Y.-C. (2020). Development of an Elastic Piezoelectric Yarn for the Application of a Muscle Patch Sensor. ACS Omega, 5(45), 29427–29438. https://doi.org/10.1021/acsomega.0c03309

[78] Giannelli, P., Calabrese, G., Frattini, G., Granato, M., & Capineri, L. (2019). A Buffered Single-Supply Charge Amplifier for High-Impedance Piezoelectric Sensors. IEEE Transactions on Instrumentation and Measurement, 68(2), 368–376. https://doi.org/10.1109/tim.2018.2849521

[79] Palmar, R., & Mancini, R. (2001). Sine-wave oscillator. https://www.ti.com/lit/an/sloa060/sloa060.pdf

[80] Stitt, R. M. (2000). Simple filter turns square waves into sine waves. https://www.ti.com/lit/an/sbfa003/sbfa003.pdf

[81] Kuphaldt, T. (2007). Lessons In Electric Circuits

[82] Witte, R. A. (2014). Spectrum and Network Measurements, ser. Electromagnetics and Radar. SciTech Publishing.

[83] Fujimoto, D., Lu, H.-H., Kumamoto, K., Tsai, S.-E., Huang, Q.-P., & Xie, J.-Y. (2019). Phase-Modulated Hybrid High-Speed Internet/WiFi/Pre-5G In-Building Networks Over SMF and PCF With GI-POF/IVLLC Transport. IEEE Access, 7, 90620–90629. https://doi.org/10.1109/access.2019.2926709

[84] All About Circuits. (n.d.). Practical guide to radio-frequency analysis and design. EETech Media. https://www.allaboutcircuits.com/assets/pdf/radio-frequency-analysis-design.pdf

[85] Gift, S. J. G., & Copeland, B. (2000) A High-Quality Mixer Circuit. West Indian Journal of Engineering, 23(1).

[86] Williams, I., & Kay, R. (n.d.) Slew Rate – 1. https://training.ti.com/system/files/docs/1221%20-%20Slew%20Rate%201%20-%20slides.pdf

[87] Wilson, G. (1990). Wien bridge oscillator with reduced amplifier gain-bandwidth product dependence. IEE Proceedings G-Circuits, Devices and Systems, 137(1), 13-15.

[88] Gotti, R., Puppe, T., Mayzlin, Y., Robinson-Tait, J., Wójtewicz, S., Gatti, D., Alsaif, B., Lamperti, M., Laporta, P., Rohde, F., Wilk, R., Leisching, P., Kaenders, W. G., & Marangoni, M. (2020). Comb-locked frequency-swept synthesizer for high

precision broadband spectroscopy. Scientific Reports, 10(1). https://doi.org/10.1038/s41598-020-59398-1

[89] Brill, D., Gaunaurd, G. C., & Überall, H. (1982). Acoustic spectroscopy. The Journal of the Acoustical Society of America, 72(3), 1067–1069. https://doi.org/10.1121/1.388217

[90] Lei, Y. (2017). Signal processing and feature extraction. In Intelligent Fault Diagnosis and Remaining Useful Life Prediction of Rotating Machinery (pp. 17–66). Elsevier. https://doi.org/10.1016/b978-0-12-811534-3.00002-0

[91] Jannson, T. (1983). Real-time Fourier transformation in dispersive optical fibers. Optics Letters, 8(4), 232. https://doi.org/10.1364/ol.8.000232

[92] Moreland, K., & Angel, E. (2003, July). The FFT on a GPU. In Proceedings of the ACM SIGGRAPH/EUROGRAPHICS conference on Graphics hardware (pp. 112-119).

[93] Damato, A. (2007). Short-time Fourier transform. Wikipedia. https://en.wikipedia.org/wiki/Short-time_Fourier_transform.

[94] Zhang, S., Yu, D., & Sheng, S. (2006, December). A Discrete STFT Processor for Real-time Spectrum Analysis. APCCAS 2006 - 2006 IEEE Asia Pacific Conference on Circuits and Systems. APCCAS 2006 - 2006 IEEE Asia Pacific Conference on Circuits and Systems. https://doi.org/10.1109/apccas.2006.342241

[95] Venkatesan, K. G. S. (2013). Comparison of CDMA & GSM Mobile Technology. Middle-East Journal of Scientific Research, 13(12), 1590-1594.

[96] Schoute, F. (1983). Dynamic Frame Length ALOHA. IEEE Transactions on Communications, 31(4), 565–568. https://doi.org/10.1109/tcom.1983.1095854

[97] Calhoun, V. D., Adali, T., Hansen, L. K., Larsen, J., & Pekar, J. J. ICA of functional MRI data: an overview, 2003. In 4th International Symposium on Independent Component Analysis: Nara, Japan.

[98] Plumbley, M. D. (2003). Algorithms for nonnegative independent component analysis. IEEE Transactions on Neural Networks, 14(3), 534–543. https://doi.org/10.1109/tnn.2003.810616

[99] Charoensak, C., & Sattar, F. (n.d.). A Single-Chip FPGA Design for Real-Time ICA-Based Blind Source Separation Algorithm. 2005 IEEE International Symposium on Circuits and Systems. 2005 IEEE International Symposium on Circuits and Systems. https://doi.org/10.1109/iscas.2005.1465962

[100] Benko, G., & Juhasz, Z. (2019, May). GPU implementation of the FastICA algorithm. 2019 42nd International Convention on Information and Communication Technology, Electronics and Microelectronics (MIPRO). 2019 42nd International Convention on Information and Communication Technology, Electronics and Microelectronics (MIPRO). https://doi.org/10.23919/mipro.2019.8757036

Vita

Ariel Slepyan received the Bachelor of Science degree in Biomedical Engineering from Johns Hopkins University in 2020. He continued his education at Johns Hopkins University's Biomedical Engineering MSE program and is entering the PhD program in Electrical and Computer Engineering. His research focuses on the development of scalable tactile sensor arrays using frequency multiplexing techniques. He has been a Teaching Assistant in multiple courses at JHU, including Principles of Biomedical Instrumentation and Biomedical Data Science Lab. His work has been presented at the 2020 conference on Biomedical Robotics and Biomechatronics (BioROB), and the 2021 conference on Neural Engineering (NER).